NASA Contractor Report 198492

High Temperature Coarsening of Cr_2Nb Precipitates in Cu-8 Cr-4 Nb Alloy

Kenneth Reed Anderson
University of California at Davis
Davis, California

June 1996

Prepared for
Lewis Research Center
Under Contract C–77166–B

National Aeronautics and
Space Administration

High Temperature Coarsening of Cr_2Nb Precipitates in Cu-8 Cr-4 Nb Alloy

BY

Kenneth Reed Anderson
B. S. (University of California, Davis) 1992

THESIS

Submitted in partial satisfaction of the requirements for the degree of

MASTER OF SCIENCE

in

Engineering

in the

OFFICE OF GRADUATE STUDIES

of the

UNIVERSITY OF CALIFORNIA

Davis

ACKNOWLEDGEMENTS

I would like to thank my parents, Darrell and Karen Anderson, for their support and encouragement throughout my undergraduate and graduate career. I would like to gratefully acknowledge the NASA/OAI Collaborative Student Summer Internship at the NASA Lewis Research Center, Cleveland, Ohio, for its vital support and providing the research opportunity which was paramount for the completion of this thesis. I would also like to extend my deepest gratitude to David L. Ellis for supplying the material, Anita Garg for her extensive help with TEM, David Hull, and Pat and Rob Dickerson, all at NASA LeRC.

I would also like to give special thanks to Professors Jeff C. Gibeling and Subhash Risbud for kindly taking part in my Thesis committee. Finally, I would like to give the greatest thanks possible to my advisor, Joanna Groza for all of her continuous guidance, support and patience of me and confidence in me.

TABLE OF CONTENTS

ABSTRACT

A new high-temperature-strength, high-conductivity Cu-Cr-Nb alloy with a Cr:Nb ratio of 2:1 was developed to achieve improved performance and durability. The Cu-8 Cr-4 Nb alloy studied has demonstrated remarkable thermal and microstructural stability after long exposures at temperatures up to 0.98 T_m. This stability was mainly attributed to the slow coarsening kinetics of the Cr_2Nb precipitates present in the alloy. At all temperatures, the microstructure consists of a bimodal and sometimes trimodal distribution of strengthening Cr_2Nb precipitates, depending on precipitation condition, i.e. from liquid or solid solution, and cooling rates. These precipitates remain in the same size range, i. e. large precipitates of approximately 1 μm, and small precipitates less than 300 nm, and effectively pin the grain boundaries thus retaining a fine grain size of 2.7 μm after 100 h at 1323 K. (A relatively small number of Cr-rich and Nb-rich particles were also present.) This grain boundary pinning and sluggish coarsening of Cr_2Nb particles explain the retention of good mechanical properties after prolonged holding at very high temperatures, e. g., 75% of the original hardness after aging for 100 h at 1273 K. Application of LSW-based coarsening models indicated that the coarsening kinetics of the large precipitates are most likely governed by grain boundary diffusion and, to a lesser extent, volume diffusion mechanisms.

1. INTRODUCTION

In the past five to ten years, Cu-Cr-Nb alloys with the Cr:Nb ratio of 2:1 developed by NASA have received special attention as the next generation of high-temperature strength high conductivity dispersion strengthened (DS) alloys [1,2]. Their retained high thermal conductivity and inherent/characteristic high temperature strength make these particular alloys prime candidates for a variety of actively cooled structures, including plasma interactive components in fusion power systems, combustion chamber liners, rocket nozzles, and heat exchangers. The strengthening is provided by the precipitation of the hard Cr_2Nb intermetallic compound, which is stable up to its congruent melting point of 2006 K and is not soluble in solid copper. The Cr:Nb ratio of 2:1 is selected such that virtually all Cr and Nb combine to form the Cr_2Nb compound to preserve the high thermal conductivity of the pure copper matrix. Fully reacting the Nb with the Cr also avoids the formation of Nb precipitates that are susceptible to hydrogen embrittlement. For this purpose, an excess amount of chromium is sometimes preferred. By using a Cr-rich Cr_2Nb precipitate, the activity of the Nb can be significantly lowered and the pressure necessary for forming niobium hydrides greatly increased [3]. Also, as evidenced by the Cu-Cr and Cu-Nb phase diagrams (see Figs. 1a and 1b), chromium and niobium have negligible solubility in Cu from 298 K up to 1200 K, which preserves the valuable thermal conductivity of copper. According to the Cr-Nb phase diagram, the Cr_2Nb compound is formed in a composition range from 62.78 to 68.08 at.% Cr (Fig. 1c), thus allowing for some compositional deviations from the Cr:Nb ratio of 2:1.

Comparison of Cu-Cr-Nb alloys with different Cr and Nb content at the same 2:1 Cr:Nb ratio indicated best overall combination of properties (e.g., conductivity, high temperature behavior, etc.) for 8 at%Cr and 4 at%Nb (Cu-8 Cr-4 Nb) composition [2]. This comparison was carried out on the initial chill block melt spun (CBMS) Cu-Cr-Nb alloys.

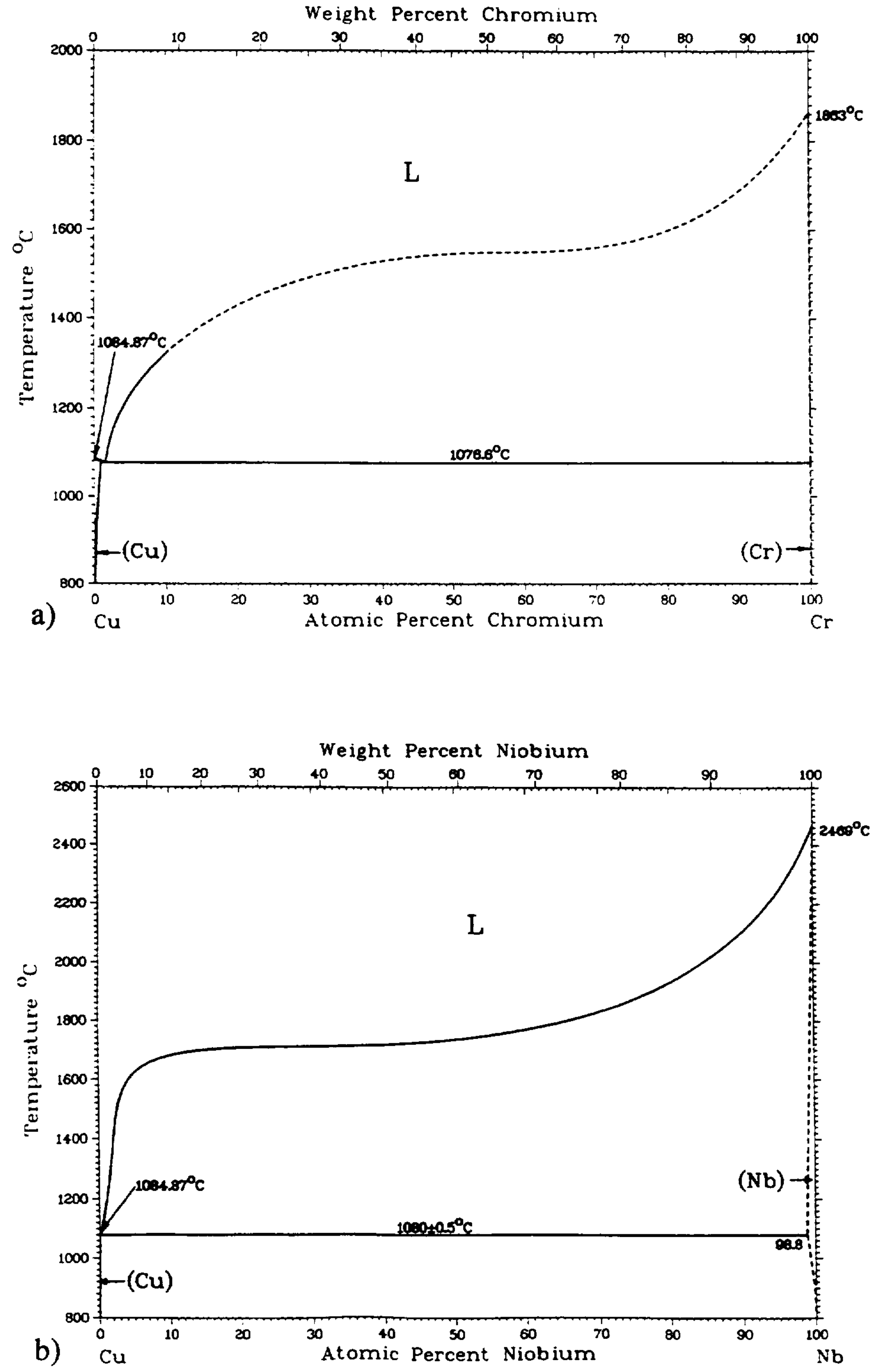

Figure 1 - a) The most recent assessment of the Cu-Cr phase diagram from [4a].
b) The most recent assessment of the Cu-Nb phase diagram from [4a].

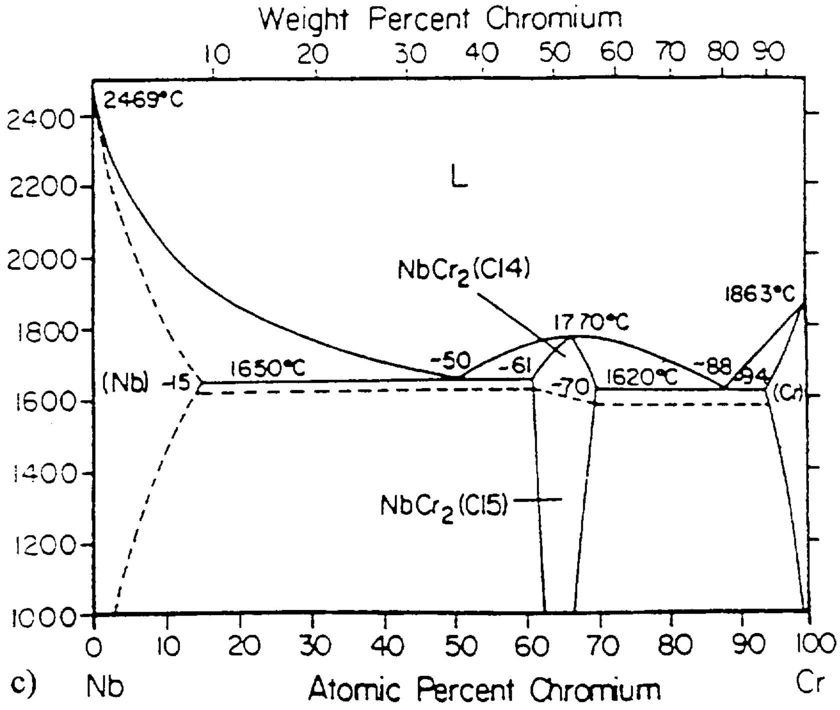

Figure 1 - c) The most recent assessment of the Nb-Cr phase diagram drawn from [4b].

In order to obtain larger quantities of Cu-8 Cr-4 Nb alloys, argon atomization was ultimately chosen as the final powder processing/production route instead of CBMS. Mechanical testing of such an atomized alloy in as-extruded and aged conditions revealed promising room and elevated temperature properties, as well as good thermal stability [1, 5, 6]. For instance, the tensile strength of Cu-8 Cr-4 Nb alloy is 426 MPa at room temperature and 100 MPa at 975 K, substantially higher than the same properties of NARloy-Z (Cu-3wt.% Ag-0.5wt.% Zr), the alloy currently used in aerospace applications. For example, the UTS at room temperature for NARloy-Z is 270 MPa and that at 975 K is ≈ 50-70 MPa. While a precipitation hardening effect was observed in Cu-8 Cr-4 Nb after short aging times, there was no significant decrease in mechanical strength after prolonged high temperature exposure. For example, the tensile strength after 100 h exposure at 973 K decreased less than 9.5% when compared to the 10 h aged specimen at the same temperature. Low cycle fatigue data at room and elevated temperatures also show a distinct advantage of Cu-8 Cr-4 Nb over NARloy-Z [6].

Details of microstructure-property relationships which substantiate the observed good thermal stability up to 973 K have been reported [5]. Further mechanical testing was performed at temperatures higher than 973 K, indicating unusually good thermal stability up to temperatures approaching the melting point, e.g.. 1325 K, or 0.98 T_m. These results are remarkable by comparison with other Cu-based DS alloys in which particle coarsening or dissolution occurs causing excessive grain growth that compromises the mechanical properties above 0.8 T_m [7]. The objective of the present work is to assess and gain understanding of this unusual high temperature behavior/stability via an examination of the particle coarsening behavior of Cr_2Nb in Cu-8 Cr-4 Nb alloy. This examination involves particle size measurements and analyses, as well as studies of microstructural features, of material aged at various conditions of temperature and time.

Particle coarsening/dissolution, or Ostwald ripening, is the primary focus since the rate at which dispersed particles increase in average size can ultimately govern the rate of degradation of superior material properties of such a DS alloy at elevated temperatures (e.g., > $0.5T_m$). In other words, study of the coarsening rate of a dispersed-particle phase is essential since the Ostwald-ripening of the dispersed phase, along with any associated grain growth, is a major factor in determining a DS alloy's resistance to degradation of its enhanced thermo-mechanical properties. Such studies of the *microstructural stability* of DS alloys is crucial, especially when considering prolonged high temperature exposure (e.g. high service/testing temperatures involving creep deformation). The driving force for the present particle coarsening study of a DS Cu alloy has now been established. But before presenting results and analyses of this study, a background review of particle coarsening is first in order.

2. PARTICLE COARSENING

2.1 THERMODYNAMICS OF PARTICLE COARSENING

Coarsening considered here is particle growth after precipitation has taken place. The driving force for this decomposition (precipitation) is the reduction in system free energy associated with a metastable supersaturated solid solution transforming into a stable two-phase mixture, as Fig. 2 shows. After this decomposition all B atoms in supersaturated α-phase have transformed by nucleation and growth into second (β) phase, leaving overall α-matrix with equilibrium concentration(s), C_e, etc., as depicted in Fig. 3.

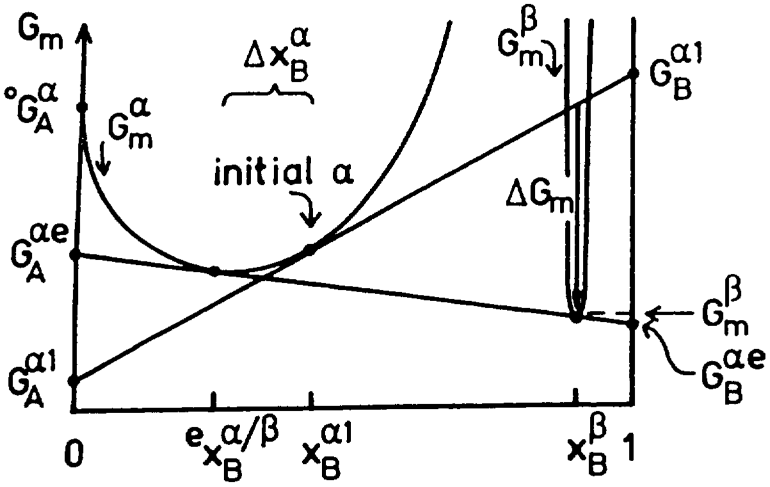

Figure 2 - Demonstration of the driving force at the start of a precipitation reaction (taken from [9]).

The thermodynamic driving force for virtually all particle coarsening is the decrease/ minimization of the total free energy, G, via the evolution of a lower overall specific particle/matrix interfacial area due to the coarser precipitates. In other words, irrespective of the mechanism which controls Ostwald ripening, it is reduction in total (surface) energy in the system which drives the reaction. That is, the system is driven by the minimization of $\Sigma\gamma A$, where γ and A are the interfacial energy and area of the respective particles. Furthermore, it has been shown by differential scanning calorimetry traces [10] that the

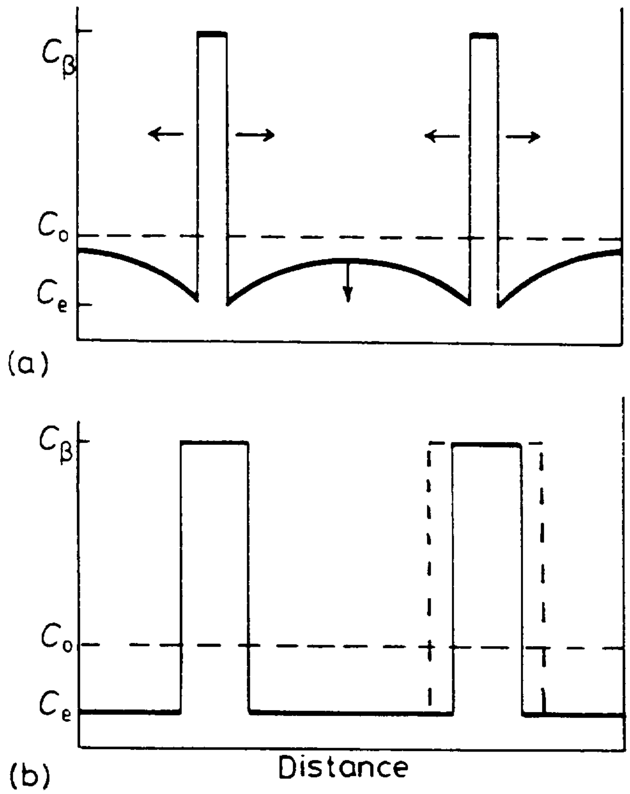

Figure 3 - a) Interference of growing precipitates due to overlapping diffusion fields at later stage of growth;
b) Precipitate growth has stopped (taken from [8]).

free energy reduction associated with decreasing total surface area (energy) is manifested by heat evolution; in other words, coarsening is an exothermic reaction.

As alluded to earlier, the microstructure of a two-phase alloy is necessarily out of equilibrium if the total interfacial free energy is not minimized. In other words a system with particles of different sizes is thermodynamically unstable due to large surface energy effects. Larger particles having lower overall surface (interfacial) area tend to grow at the expense of smaller precipitates, which tend to dissolve and shrink, thus giving an overall lower system free energy. Therefore a high density of small precipitates will tend to coarsen into a relatively lower density of larger particles. The thermal stability of microstructure and, of coarse, the retention of strength at elevated temperatures, are obviously enhanced by slowing this coarsening process.

2.1.1 Gibbs-Thomson Effect

As mentioned by Porter and Easterling [8, p.315], in any precipitation hardened material there will be a range of particle sizes due to differences in the nucleation time and growth rates. Due to a capillarity effect or the Gibbs-Thomson effect, the solute (B) concentration in the matrix adjacent to a particle will increase as the radius of curvature decreases. This follows from the fact that solute solubility depends exponentially on a free energy difference, ΔG. This Gibbs free energy difference is increased by the factor $2\gamma/r$ -- which is due to associated interfacial energies and radii of particles -- which subsequently increases the solute solubility [8]. Figure 4 below shows two adjacent spherical particles with different diameters. The smaller particle will experience a greater increase in free energy (larger capillarity effect, $2\gamma/r$) than the larger particle - compared to a particle of infinite radius - causing the enhanced solute concentration in the matrix at the smaller particle. This effect of $2\gamma/r$ on solubility is depicted graphically in Figs. 5 and 6 below and given in the following equation form:

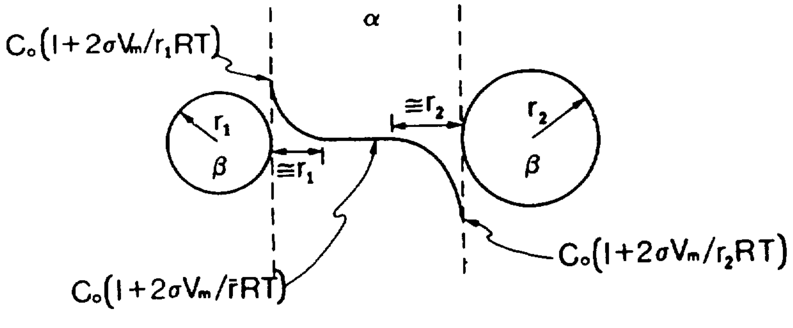

Figure 4 - Two β particles (radii r_1 and r_2) in an α matrix. Local equilibrium is assumed to exist at the respective particle-matrix interfaces so that $C(r_1) > C(r) > C(r_2)$. This leads to transfer of β atoms to the matrix from the smaller particle and its subsequent dissolution. The opposite process occurs in the region of the matrix/large particle interface. The characteristic diffusion distance is proportional to the particle radius (taken from [11]).

$$C_r = C_{e,\infty}\left(1 + \frac{2\gamma V_m}{rRT}\right) \qquad (1)$$

where C_r = the equilibrium solubility of a particle of radius r (m);

$C_{e,\infty}$ = the equilibrium solubility of infinite radius;

γ = the dispersoid/matrix interfacial energy in J/m^2;

V_m = the molar volume of the particle in m^3/mole;

R = 8.314 J/mol·K; and

T = absolute temperature in degrees Kelvin (K).

2.1.2 Induced Atom Fluxes (Concentration Gradients)

Coarsening occurs as a result of the concentration gradient that develops between particles of different sizes (Gibbs-Thomson effect, Fig. 4). As Fig. 5 shows, smaller particles do indeed increase the free energy relative to the larger particles, thus affecting

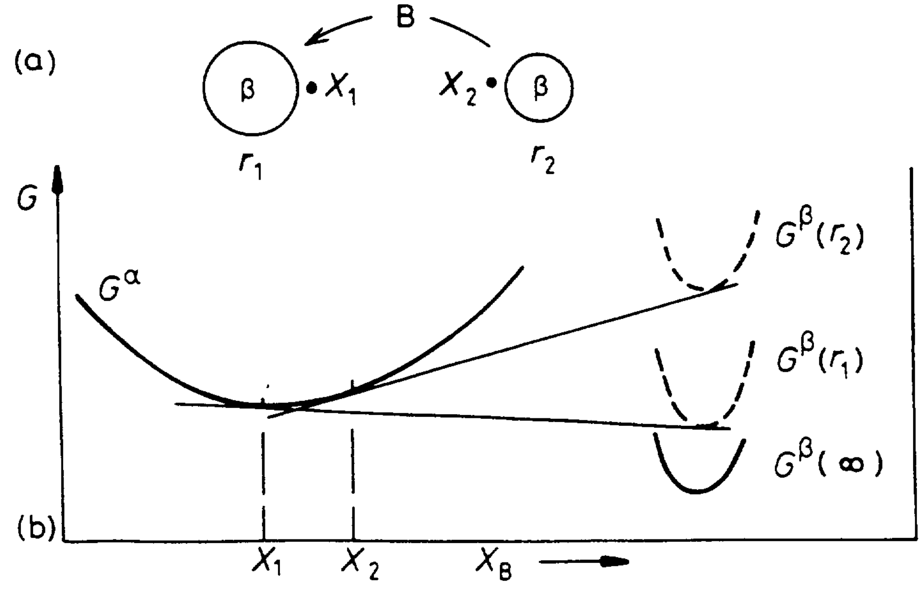

Figure 5 - a) and b) The origin of particle coarsening. β with a small radius of curvature (r_2) has a higher molar free energy than β with a large radius of curvature (r_1). The concentration of solute is therefore highest outside the smallest particles (taken from [8]).

local composition differently which, of course, induces interparticle diffusion flow due to effective concentration gradient. For example, the flux of B atoms can be expressed as:

$$J_B = D_B\left(\frac{\Delta C}{\Delta x}\right)_B \tag{2}$$

where D_B = the diffusivity of B in α in cm^2/s;

ΔC = a change in concentration in atoms/cm^3; and

Δx = a change in distance (or interval) in cm.

D_B can be further expressed in the following expanded Arrhenius form:

$$D_B = D_{o,B}\exp\left(-\frac{Q_B}{RT}\right)cm^2/s, \tag{3}$$

where D_o = pre-exponential material constant in cm^2/s;

Q = the activation energy for diffusion in J/mol; and

Figure 6 describes more definitively the effects of dissolving and growing precipitates on the molar free energy of the system. In fact, it shows directly 1) the difference of $2\gamma/r$

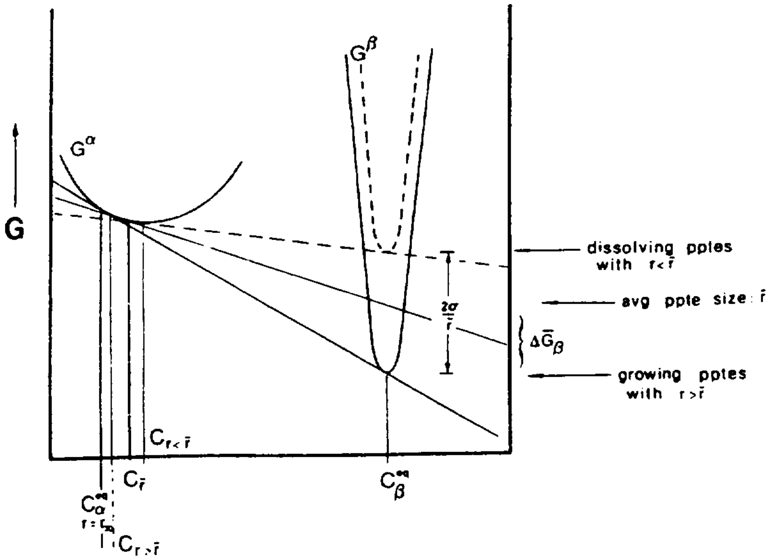

Figure 6 - Free energy versus composition diagram illustrating the precipitation of β from an α matrix. The two cases illustrated can be imagined to correspond to a growing or dissolving precipitate (taken from [11]).

between the free energy of particles having smaller and larger radii than the average; and 2) how the respective interfacial solute concentrations relate to those for $r = \infty$ and $r = \bar{r}$.

The fundamental thermodynamic driving force for the interparticle diffusion flow can also be taken as the chemical potential differences, $\Delta\mu_B$, established among particles. The chemical potential (of B in matrix), μ_B, is also the partial molar free energy of B and can be defined as the change in Gibbs free energy with change in concentration of B [8]. Local differences in μ_B arise due to differences in curvature (radii) of particles since μ_B depends on composition [8] and local compositions depend on particle radii, as Fig. 6 shows. Therefore, the flux of B atoms can also be expressed in the following way [11]:

$$J_B \cong \frac{D_B C_B}{RT}\left(\frac{\Delta\mu}{\Delta x}\right)_B \tag{4}$$

where C_B = concentration of B in atoms/cm^3 and

$\Delta\mu$ = change in chemical potential, in J/mol.

Fig. 6 also shows that reducing the interfacial energy also means reducing the partial molar free energy (chemical potential) difference, $\Delta\overline{G}$ $(\Delta\mu)$, which lowers the gradient. Finally, it can be said (as Voorhees and Glicksman [12] do) that phase coarsening can occur any time when interfaces with disparate curvatures are in close enough proximity to allow the chemical potential gradient to drive a significant flow between particles.

Thus, as the above discussion and figures show, this Gibbs-Thomson effect induces ***concentration/chemical potential gradients*** in the matrix which will cause solute to diffuse in the direction of the largest particles away from the smallest such that the small particles shrink and disappear while large particles grow. (Figs. 5b and 6 effectively show the ***thermodynamics*** or free energy driving force behind particle coarsening.) The overall result is that the total number of particles decreases and the mean radius, r increases with time. But now the other issue of coarsening deserving discussion is of course the ***kinetics*** governing particle coarsening.

2.2 COARSENING KINETICS MODELS –LSW-THEORY

The first real efforts to theoretically and quantitatively describe the coarsening behavior of a dispersed second phase in a parent matrix were made by Lifshitz and Slyozov [13] and Wagner [14]. Although the LSW theory was developed to model the kinetics of precipitate growth from supersaturated solid solutions after the completion of nucleation, it may also apply to other methods of particle incorporation (e.g. mechanical alloying and internal oxidation) as well as to coarsening of grains in liquid-phase sintering [15-18] and to the coarsening of pores in solid state sintering [19,20]. It was also based on a zero volume percent of coarsening phase approximation. One important prediction of the LSW theory is the existence and specific shape of an asymptotic particle size distribution (PSD), or histogram. In fact, LSW theory 'predicts' this interesting phenomenon of a "quasi steady state" particle-size distribution evolving no matter what the initial distribution (later shown in Fig. 11).

2.2.1 *Volume Diffusion Controlled*

Another important prediction of the LSW theory involves coarsening which is volume diffusion controlled (VDC). The coarsening rate of incoherent particles will be effectively VDC since the interface mobility of such particle/matrix interfaces is very high [8]. LSW predicts that the average particle radius is proportional to $t^{1/3}$ (or $\bar{r}^3 \propto t$) with the constant of proportionality, i.e. the rate constant, dependent only on material parameters [12]. The exact form of this relationship as derived for *spherical* particles usually takes the following form [21]:

$$\bar{r}_t^3 - \bar{r}_o^3 = \frac{8\gamma V_m D C_{e,\infty}}{9RT}\mathrm{t} = \mathrm{Kt} \qquad (5)$$

where $\bar{r}_t$ = average particle radius at time t;

$\bar{r}_o$ = average particle radius at the onset of coarsening;

D = diffusivity of rate controlling solute in the matrix; and

$C_{e,\infty}$ = equilibrium solubility of the rate-controlling solute in the matrix.

The numerical factor of 8/9 in Eqn. (5) comes about since this LSW equation for the rate of change of mean radius of the dispersion with time requires that the PSD has assumed a specific form which is characteristic of the coarsening of precipitates at the time $t = 0$ and that the supersaturation of the matrix has decreased to a level where equilibrium exists at the matrix/particle interface [22]. As an aside, Voorhees and Glicksman have expressed amazement at the idea that particles originally distributed randomly throughout a matrix will spontaneously coarsen such that their sizes collectively tend toward a fixed (asymptotic) size distribution (relative to the average and after a sufficiently long time) and display an average which grows as the cube root of time [12].

Another r^3 - t relation has been established in a study by Cochardt of thermal stability of dispersion hardened alloys from the perspective of the time necessary to dissolve small particles. Starting with the Gibbs-Thomson equation and using steady state approximation, Cochardt obtained the following equation [11]:

$$t = \frac{\rho^2 RT r_o^3}{3.6 M \gamma D C_\infty} f \qquad (6)$$

Equation (6) represents the time necessary for a particle of radius r_o to dissolve. In this equation ρ is the particle density, M is the molecular weight of particle, and f is a function of particle size and solute diffusion distances. ($f \approx 1$ for low particle volume fractions, e.g. <0.05.) Table 1 below shows his results for various dispersoids in various matrices. Note the large time for the case of Al_2O_3 in Ni-4Al. Cochardt attributed this to the negligible capillarity effect due to the very low level of solubility in the matrix, thus, giving a negligible diffusion gradient for coarsening to occur.

Table I. Time for Dispersoids to Dissolve in Selected High Temperature Alloys [11]

Dispersoid	Matrix*	T (K)	Diffusing Element	t (sec/hours)
Ni_3Al	Ni-4 Al	1000	Al	$10^2/0.03$
Al_2O_3	Ni-4 Al	1000	O	$10^{11}/2.8\times10^7$
Al_2O_3	Ni-8 Al	1500	O	$10^6/278$
Fe_3C	Fe-0.025 C	995	C	$10^1/2.8\times10^{-4}$
TiC	Ni-0.1 C	1000	C	$10^2/0.3$
TiN	Ni	1000	N	$10^4/2.8$

*Compositions are in weight percent.

2.2.2 *Grain-Boundary Diffusion Controlled*

When grain-boundary (GB) diffusion governs the coarsening process, the relationship of particle size to time becomes $\bar{r}^4 \propto t$ [21], that is:

$$\bar{r}_t^4 - \bar{r}_o^4 = \frac{9\delta\gamma W_m D_{gb} C_{e,\infty,gb}}{32ABRT} t = k't \qquad (7)$$

where δ = grain boundary thickness;

D_{gb} = grain boundary diffusivity of rate-controlling species;

$C_{e,\infty,gb}$ = equilibrium solubility of the rate-controlling species in the grain boundary;

$A = 2/3 - \gamma_b/2\gamma + (1/3)(\gamma_b/2\gamma)^3$;

$B = (1/2)\ln(1/f)$;

γ_b = grain boundary energy; and

f = fraction of grain boundary covered by dispersoids.

Figure 7 shows how grain-boundary diffusion can enhance coarsening of particles at GBs.

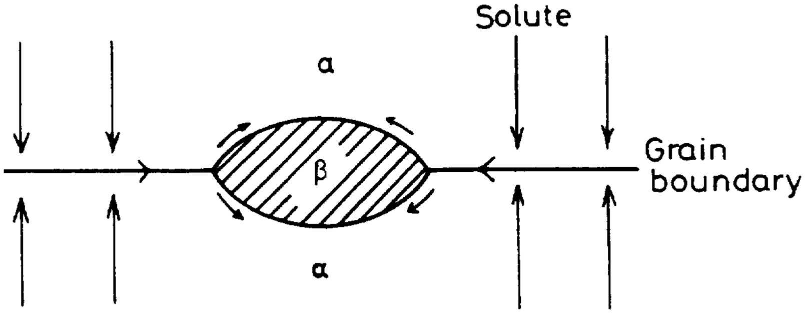

Figure 7 - Grain-boundary diffusion can lead to a rapid lengthening and thickening of grain boundary precipitates (taken from [8]).

Both Eqns. (5) and (7) and Cochardt's expression show a direct dependence on interfacial energy, γ, diffusivity, D, and solubility, C. ***This directly leads to strong desire to minimize these three parameters in order to make the coarsening kinetics as sluggish as possible***. Furthermore, since D and C (from equilibrium phase diagram) increase exponentially with temperature, the coarsening rate will also increase rapidly with increasing temperature (see Fig. 8 below). Obviously the lowest service temperature possible should be sought. This again emphasizes the importance of designing an alloy system with negligible solubility and low diffusivity of the rate-controlling solute.

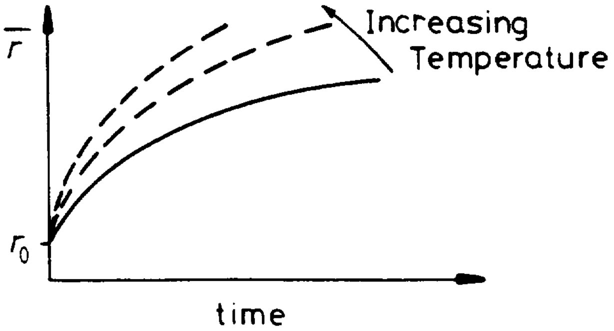

Figure 8 - Schematic diagram illustrating how the mean particle radius, $\bar{r}$, increases with time at different temperatures (taken from [8]).

2.2.3 Interface Reaction Controlled

Finally, a third version of the LSW formula is for the situation when coarsening is governed by an interface reaction controlled (IRC) process. This is the condition when the rate limiting step is atomic attachment or detachment at the particle/matrix interface, i.e. the growth process is the transfer (flux) of the dispersoid species across the particle-matrix interface. The coarsening rate of coherent and semicoherent particles will be effectively IRC since the interface mobility of such particle/matrix interfaces is very low [8]. For this case a linear relationship between the average radius squared and the coarsening rate was shown by Wagner [14] to be described as:

$$\bar{r}_t^2 - \bar{r}_o^2 = \frac{64\gamma V_m C_{e,\infty} k}{81RT} \mathrm{t} = \mathrm{K't} \qquad (8)$$

where k is the interphase boundary reaction constant. Coarsening of coherent or partially coherent particles is usually modeled as a ledge migration mechanism, which has been described by Shiflet and Hawk [11]. They point out that in most solid-solid systems precipitates develop specific crystallographic orientation relationships with the parent matrix due to constraints imposed by nucleation. These orientation relationships often result in the formation of low energy fully or partially coherent interfaces. The growth kinetics (or dissolution) of such an interface is accomplished through the lateral migration of stepped terraces, or ledges (Figures 9 & 10). The growth kinetics of these interfaces depend on ledge nucleation kinetics, ledge height, volume diffusion to the interface, and the complicated diffusion and elastic fields near the ledge.

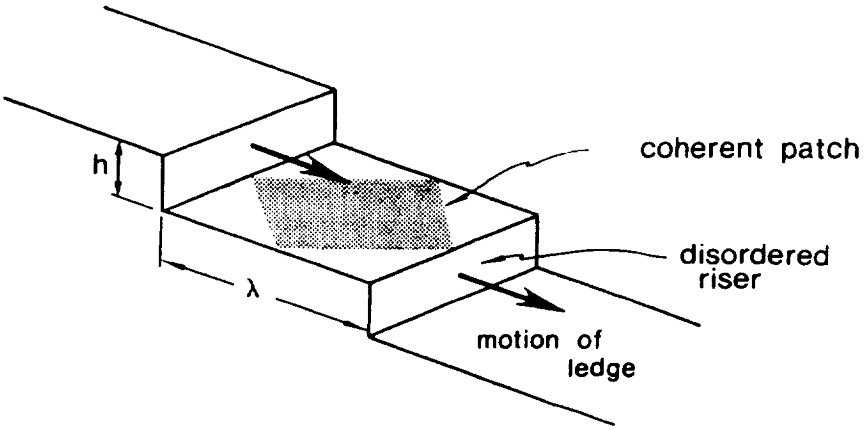

Figure 9 - Schematic representation of ledge migration controlled coarsening model (taken from [11]).

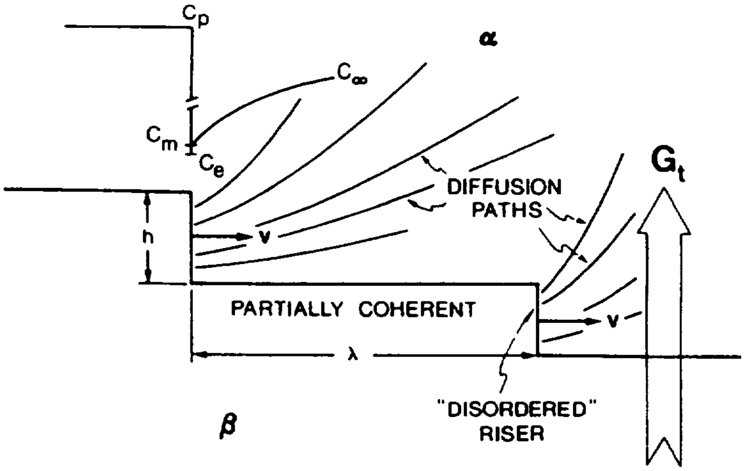

Figure 10 - Schematic of interfacial ledges existing at the interface between the matrix and a precipitate. The ledges are of height h and separated by a distance λ. In the case illustrated here, atoms attach to the precipitate β at the ledges resulting in the ledges moving with a lateral velocity v. The β particle grows into the α-matrix at a rate of G_t (taken from [11]).

The growth rate of the β particle into the α-matrix is given as [11]:

$$G_t = (h/\lambda)v \tag{9}$$

where h is the ledge height, λ is the ledge spacing, and v is given as

$$v = \frac{D}{\alpha h} \cdot \frac{C_\infty - C_e}{C_p - C_e} \tag{10}$$

where α is an effective diffusion distance. The growth rate expression assumes that the average value of the step spacing, λ, is large enough so that the step velocity is not altered due to the presence of neighboring steps. The main ledge sources (nucleation sites) result from (1) two-dimensional nucleation; (2) dislocations, either interphase or intruder type; and (3) boundary dislocations [11]. In general, ledge heights and spacings are unpredictable. As Shiflet and Hawk state, from a practical point of view, it would be useful to understand the mechanistics of ledge nucleation, for without ledges the coarsening of partially coherent precipitates would be effectively halted.

Finally, it can be noted here that if diffusion and interface controlled processes occur simultaneously then none of the above formulas will give a complete (or accurate) description of the coarsening kinetic behavior, which could help explain disagreement between experimental results and theoretical (LSW) prediction(s). As discussed next, the origin of the LSW expression(s) leads to other likely reasons for such disagreements.

2.3 MODIFICATIONS TO LSW THEORY

Originally, the LSW coarsening prediction was developed for ***infinitely dilute liquid*** phase systems. This could also definitely help explain deviations or apparent disagreements usually found between experimental results and the LSW prediction. Possible explanations for such disagreements necessarily include, among others, the LSW theory neglecting a finite particle volume fraction and much of the difficulty of having crystalline precipitates in a solid matrix, such as induced strain fields that are not present in liquid phases. Voorhees and Glicksman [12] state that "volume fraction dependence arises form particle-particle interactions which, intuitively, should permit faster diffusional transfer among particles by virtue of their finite separation." Various modifications to the LSW theory incorporating finite (increasing) volume fraction effects have been proposed by a number of investigators. For example, Ardell [23] has modified the diffusion equation based on volume fraction effects and a more realistic diffusion geometry which takes into account overlapping diffusion fields (see Fig. 11).

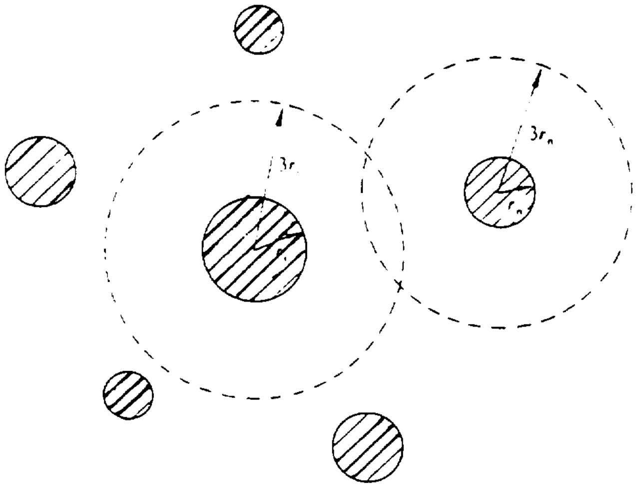

Figure 11 - An array of precipitates with a non-negligible volume fraction (f_v) such that the distances between precipitates is only somewhat larger than the mean precipitate radius (taken from [23]).

In this modified theory the rate constant, *k*, is very sensitive to volume fraction (see Fig. 12 below). Ardell basically added a multiplying parameter, k_m, to the VDC expression of LSW to account for volume fraction, e.g. $k_m = 2$ for $f_v = .01$, 5 for $f_v = .07$, etc. Also, as Figure 13 below depicts, Ardell predicts a broader PSD for finite volume fractions, f_v, than does LSW for $f_v = 0$. Voorhees and Glicksman [12] developed a modified theory based on multi-particle diffusion while Davies *et al.* [25] take into account coalescence, or encounters (impingements) between particles, a volume-fraction effect (LSEM - encounter modified). Finally, Brailsford and Wynblatt [26] developed a self-consistent (BWSC) and encounter modified (BWEM) theory. These other modified theories predict less sensitivity of k to volume fraction, as Fig. 12 shows. (Also, taking into account volume fraction predicts a broader PSD, as represented in Fig. 13.)

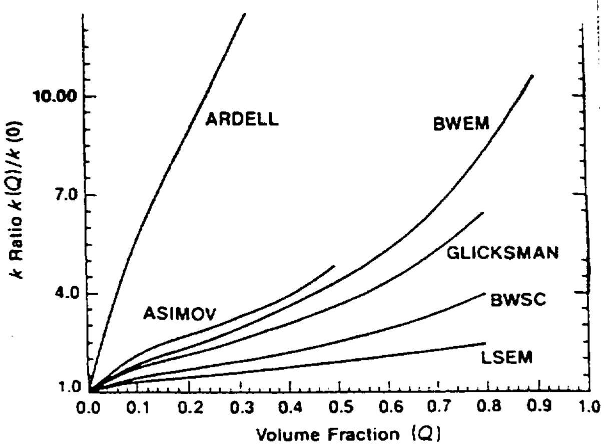

Figure 12 - Variation of *k* ratio with volume fraction according to various theories (taken from [24]).

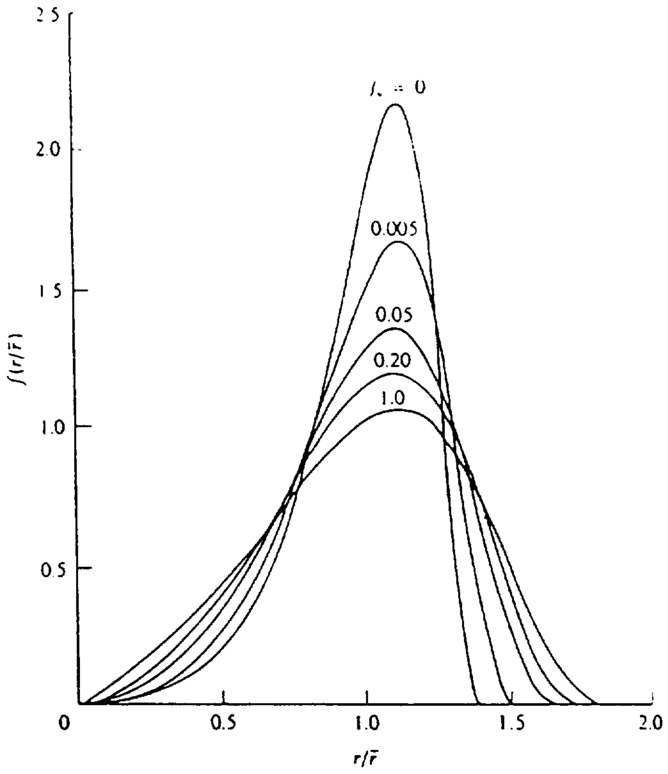

Figure 13 - Predicted distribution of particle sizes as reduced radii $r/\bar{r}$ during diffusion-controlled coarsening for a range of volume fractions (f_v) from 0 to 1.0 (taken from [23]).

Figure 12 also shows that the variation of *k* predicted by the various theories at low volume fractions ($<20\%$) is relatively small. At small volume fractions it is difficult to observe experimentally the variation of *k* with volume fraction. In fact Seno *et al.* [17,18] concluded from their coarsening studies of cobalt precipitates in Cu-Co alloys (0.69 vol% to 3.64 vol%) that the *k* value is effectively independent of volume fraction. Finally, based on their coarsening studies of $FeNiAl_9$ precipitates in aluminum, Premkumar *et al.* concluded that the effect of dispersoid volume fraction on coarsening, i.e. *k*, via the grain boundary diffusion model is higher than that via the bulk diffusion model [10].

Finally, as mentioned earlier, besides volume-fraction effects, the LSW theory does ***not*** account for local effects of particles on the solid matrix and, more importantly, the resulting effects on coarsening kinetics. Local effects on matrix and thus the **coarsening kinetics** include the anisotropy of structure between precipitate and matrix, the elastic (strain energy) effects of having a precipitate embedded in the matrix, and diffusional interaction effects due to the strain field generated by the precipitate. Overlapping strain fields and resulting overlapping diffusion fields (like in Fig. 11) may alter precipitate morphologies and thus influence transformation kinetics, owing to the dependence of the bulk equilibrium concentration fields on the local strain field [11]. Overlapping diffusion fields can also lead to coalescence. Studies such as those by Eshelby [27] and Johnson and Voorhees [28] show that the stress field associated with material defects and second phase particles can affect the equilibrium solute concentration distribution in solids. Moreover, they emphasize that this stress field can redistribute solute atoms in the matrix and thus influence the microstructure by modifying the morphology of isolated precipitates and by changing the coarsening kinetics during a phase transformation. Finally, non-spherical dispersoids can alter the diffusion field surrounding the particles and thus the coarsening rate.

The goal of this present study is to apply one or more models or formulas of the LSW theory presented above to the coarsening behavior of Cu-8 Cr-4 Nb. Thus, an attempt is made to determine such parameters as K, k′, and K′, which have not been calculated or empirically determined for this system as of yet. Gaining an understanding of what mechanisms govern the particle/microstructural stability of this promising Cu-8 Cr-4 Nb alloy is key for its ultimate potential for vital applications in aerospace/energy systems.

3. AGING/COARSENING BEHAVIOR OF Cu-8 Cr-4 Nb ALLOY

3.1 EXPERIMENTAL PROCEDURE

3.1.1 Materials

The samples used in the present investigation were from Cu-8 Cr-4 Nb bars produced by extruding cans of the powder. The chemical composition of the atomized powder supplied by Special Metals, Inc. was 6.5 wt% (7.97 at.%) Cr and 5.5 wt% (3.77 at.%) Nb with 260 ppm oxygen. All samples were made from Cu-8 Cr-4 Nb powder less than 106 μm in diameter which was canned in 5.08 cm diameter mild steel cans. The cans were extruded at 1133 K using a round die with 16:1 reduction in area. The final diameter of the extruded can was approximately 12.7 mm with a Cu-8 Cr-4 Nb core approximately 9.5 mm in diameter.

The extruded specimens were heat treated for 1, 10, 50 and 100 hours at 1073, 1173, 1273 and 1323 K. Air cooling at about 4 K/s was used for all specimens except for the 1323 K heat treatment. In the latter case, furnace cooling at about 1 K/s was used. The copper materials remained in the steel cans during the entire heating cycle. Diffusion of Fe into the alloy resulted in the formation of a Cr-Fe rich diffusion zone near the can/alloy interface [6]. The diffusion zone appeared to be limited to a few hundred nanometers at most. During machining the diffusion zone was completely removed. Microscopic examinations of the aged samples were undertaken in regions close to the center of the samples to avoid any effects of the diffusion zone.

3.1.2 Specimen Preparation and Analytical Techniques

As-atomized powders, as-extruded, and extruded and heat treated specimens were mounted and prepared by standard metallographic techniques for optical microscopy. A solution of 20 ml 3% hydrogen peroxide, 25 ml ammonium hydroxide, 25 ml distilled water, and four pellets of sodium hydroxide at room temperature was used for etching [2].

Samples for transmission electron microscopy (TEM) were cut perpendicular to the extrusion direction. The samples were mechanically thinned to ~125 μm using a Gatan lapping fixture. The final electrolytic thinning was performed using a methanol-20 % nitric acid bath at a temperature below 220 K and applying 10-15 V to the samples. Most thin foils revealed oxide and/or debris formation and redeposition during electrolytic thinning. These foils were further cleaned in a Gatan ion mill using 5 keV argon ions and a current of 0.5 mA.

For TEM analysis, a Philips EM400T electron microscope operated at 120 kV was used. The precipitates were characterized using convergent beam analysis, SAD patterns and XEDS spectra. Particle identification and counting was performed using TEM for small particles and SEM for large particles. At least 200 particles per specimen were counted. Particle measurements of TEM and SEM images were done using a Leica Quantimet 500 Image Analysis System. In addition, Vickers microhardness (HV) measurements, with 100g load and 10 second dwell time have been made for 100 h treatments between 973 and 1323 K.

3.2 RESULTS AND OBSERVATIONS

3.2.1 Precipitate Identification, Structure and Morphology

The predominant second phase identified was stoichiometrically desired Cr_2Nb precipitates. Electron diffraction (Appendix 1) revealed that the Cr_2Nb precipitates in this Cu-8 Cr-4Nb alloy are predominantly the lower temperature C15 Laves fcc phase -- with unit cell. As an aside description of this precipitate phase, the Laves phases (C14, C15, C36) are the most common structural types amongst the intermetallics. Metallic compounds tend to form with close packing of atoms, high atomic symmetry, and metallic nature of bonding [29]. Laves phases satisfy these conditions more efficiently than other intermetallic structure types. The highest configurational and symmetrical arrangement of atoms in the AB_2 Laves phases requires $r_A/r_B \approx 1.1 - 1.6$ [29]. In the present case, $r_{Nb}/r_{Cr} = 1.43nm/1.25nm \approx 1.144$. This positioning of atoms results in four layer stacking sequences in the close packed directions, i.e. XYZ....where X, Y, and Z represent closed-packed layers, similar to an fcc structure; however each layer is composed of four interpenetrating atomic layers [30].

A bimodal, sometimes trimodal precipitate size distribution was typically observed in all studied specimens (Fig. 14). The largest particles are formed congruently from the melt and were therefore considered "primary" particles (A in Fig. 14). Many of these primary particles are observed at grain boundaries and triple points (Fig. 14b). The secondary particles (B and C in Fig. 14a and 14c) are those which precipitate from solid solution during aging treatments. Consequently they are usually up to an order of magnitude smaller than primary particles and exhibit a roughly spherical shape. The trimodal particle distribution is characteristic for heat treatments at very high temperatures followed by furnace cooling (Fig. 14c). For this case, the secondary Cr_2Nb particles may be distinctively characterized as coarse (hundreds of nanometers - B in Fig. 14c) and fine (less than 100 nm - C in Fig. 14c).

The frequently observed faults of the Cr_2Nb particles (pointed out in Fig. 14a) were identified as twins on the {111} planes [31]. These faults are crystallographically-aligned and very closely resemble the twin faults as identified by Thoma and Perepezko [3]. They consider these faults typical for the polytype Laves phases. For the majority of the Cr_2Nb precipitates, the Cr:Nb ratio of 2:1 was confirmed by XEDS measurements. Occasionally, some small fcc particles exhibit a Cr:Nb ratio of 1:1. Preliminary XEDS analysis indicated these particles also contain oxygen. More work is necessary to identify these compounds and structures.

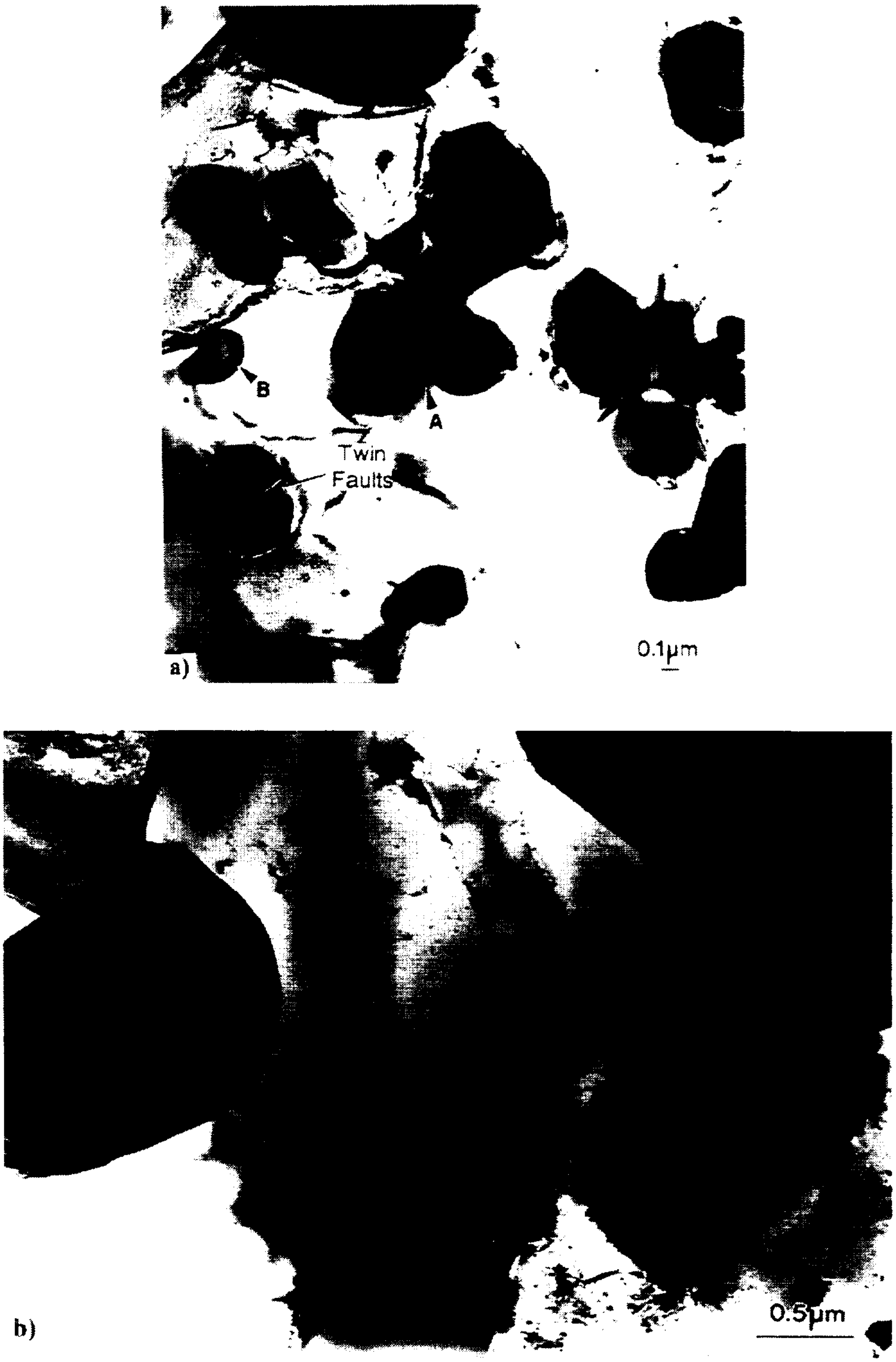

Figure 14 -Bimodal particle distribution in Cu-8 Cr-4 Nb alloy after aging at 1323 K for a) 1 h and b) 50 h. (c) Trimodal distribution after aging at 1323 K - 50 h.

Figure 14 -Bimodal particle distribution in Cu-8 Cr-4 Nb alloy after aging at 1323 K for a) 1 h and b) 50 h. (c) Trimodal distribution after aging at 1323 K - 50 h.

In addition to Cr_2Nb precipitates, Cu-8 Cr-4 Nb alloys contain some Nb-rich and Cr-rich precipitates, especially when heat treated above 1200 K (Fig. 15). Most of these particles are situated at grain boundaries or triple points. Generally, Cr-rich particles are several hundred nanometers in diameter (Fig. 15a) and larger than Nb-rich particles, which invariably reach no more than 100 nm in size, even with extreme aging conditions (Fig. 15b). Usually, the Nb-rich particle size is less than 40-50 nm. As seen in Fig. 15a, Cr-rich particles are characterized by a 'grainy' sub-structure (contrast) that was used for their initial identification. XEDS spectra of Cr-rich and Nb-rich particles are shown in Fig. 16b and 16c. For comparison, Fig. 16a shows a typical spectrum for stoichiometric Cr_2Nb. Based on the chemistry of the alloy which was purposefully Cr-rich to react all the Nb, elemental Cr precipitates were expected. XEDS analysis indicated Cr-rich precipitates contained more than 96 at.% Cr and frequently 98-99.5 at.% Cr. Convergent beam analysis of Cr-rich particles confirmed the presence of bcc Cr with a lattice parameter of 0.274 nm. In contrast, the Nb-rich particles usually contain 75-96 at.% Nb and were identified by Garg as NbO with a simple cubic structure and a lattice parameter of 0.421 nm [31].

Figure 15 - TEM micrographs showing a) Cr-rich particle (aged at 1173 K - 10 h); b) Nb-rich particle (aged at 1323 K - 100 h).

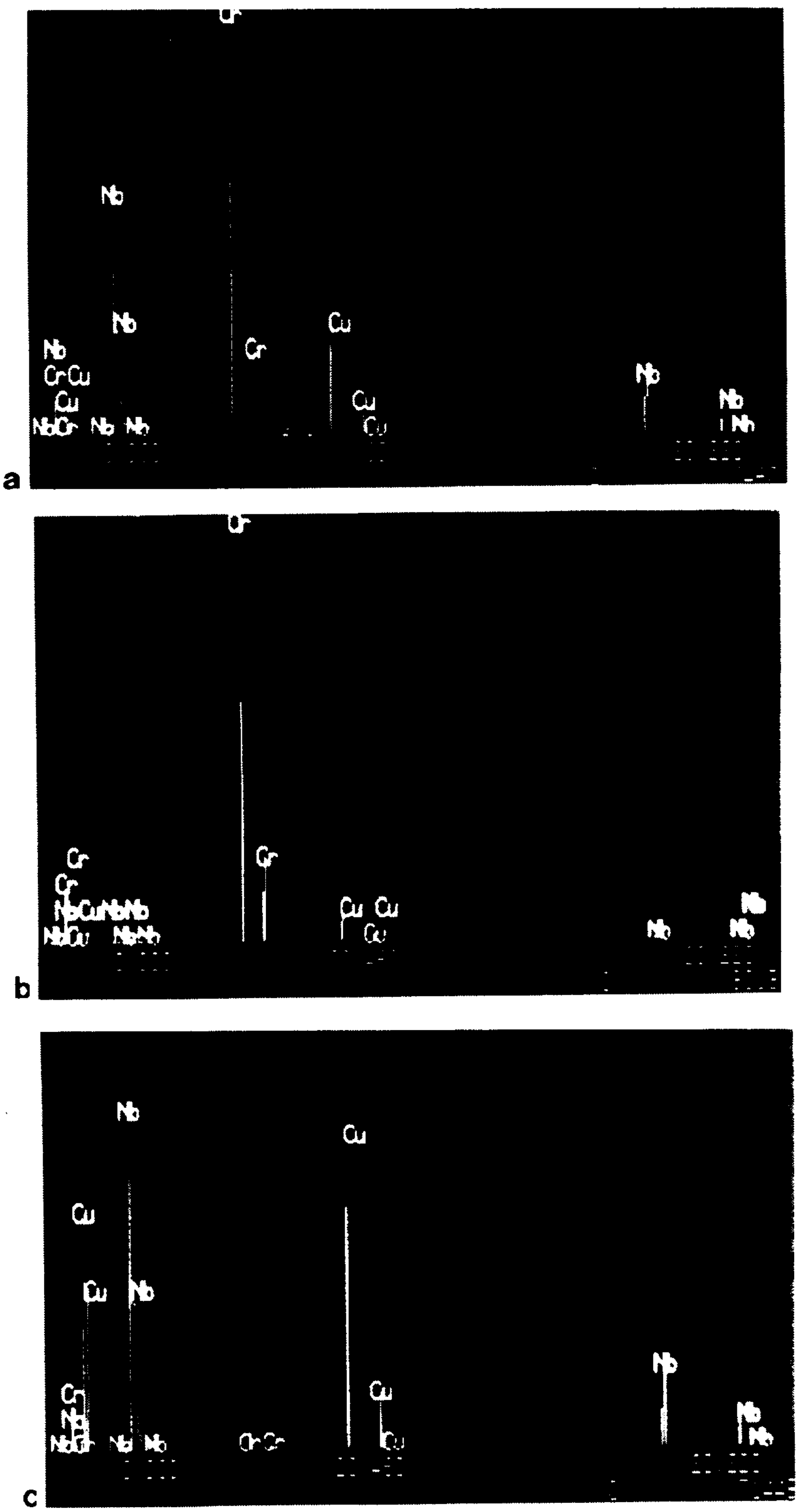

Figure 16 - XEDS Spectra of a) typical Cr_2Nb precipitate; b) Cr-rich particle (aged at 1173 K - 50 h); and c) Nb-rich particle (aged at 1173 K - 10 h).

Preliminary semi-quantitative measurements indicated an increase of the number of Nb-rich particles with increasing temperature and longer annealing times. For example, the majority of the finest particles were NbO at 1323 K, while only about 30% of the finest particles were Nb-rich at 1173 K. This percent was even smaller (around 20%) at lower temperatures (973 K). The number of Cr-rich particles amounted to a small fraction (<5 %) of total particles and varied little with temperature based on general TEM observations rather than particle counting. Further work is required to gain a more quantitative assessment of Cr-rich and Nb-rich particles.

3.2.2 Cr$_2$Nb Precipitate Coarsening

Figures 17 and 18 show the particle size histograms for small precipitates (up to 300 nm) after aging the alloy at 1173 K for 1, 10, and 100 hours and at 1323 K for 1, 10, and 50 hours, respectively. The average particle size is indicated for each aging condition. At 1173 K, the particle size increased after aging 10 h but decreased after aging 100 hours. At 1323 K, the secondary particle size decreased with annealing time due to particles dissolving into the matrix *via* coarsening and (above solvus) resolution mechanisms. (Additional nucleation is ruled out as a contributor to this particle size decrease since it has been shown that the nucleation and growth processes of Cr$_2$Nb particles have ceased after 1 h aging [5]). At this temperature, the finest particles, i.e. <40-50 nm, were not taken into account for the above histograms since they presumably comprise of a significant number of Nb-rich particles. Also, Cr-rich particles were effectively excluded by their appearance. Aging at 773 and 973 K also resulted in a decrease in the average secondary precipitate size compared to the as-extruded condition. In this case, the decrease was due to precipitation of new fine precipitates from the supersaturated solid solution formed during extrusion at 1133 K [5]. These fine precipitates which did not coarsen much following nucleation shifted the particle size distributions towards finer sizes and decreased the average size of the secondary precipitates.

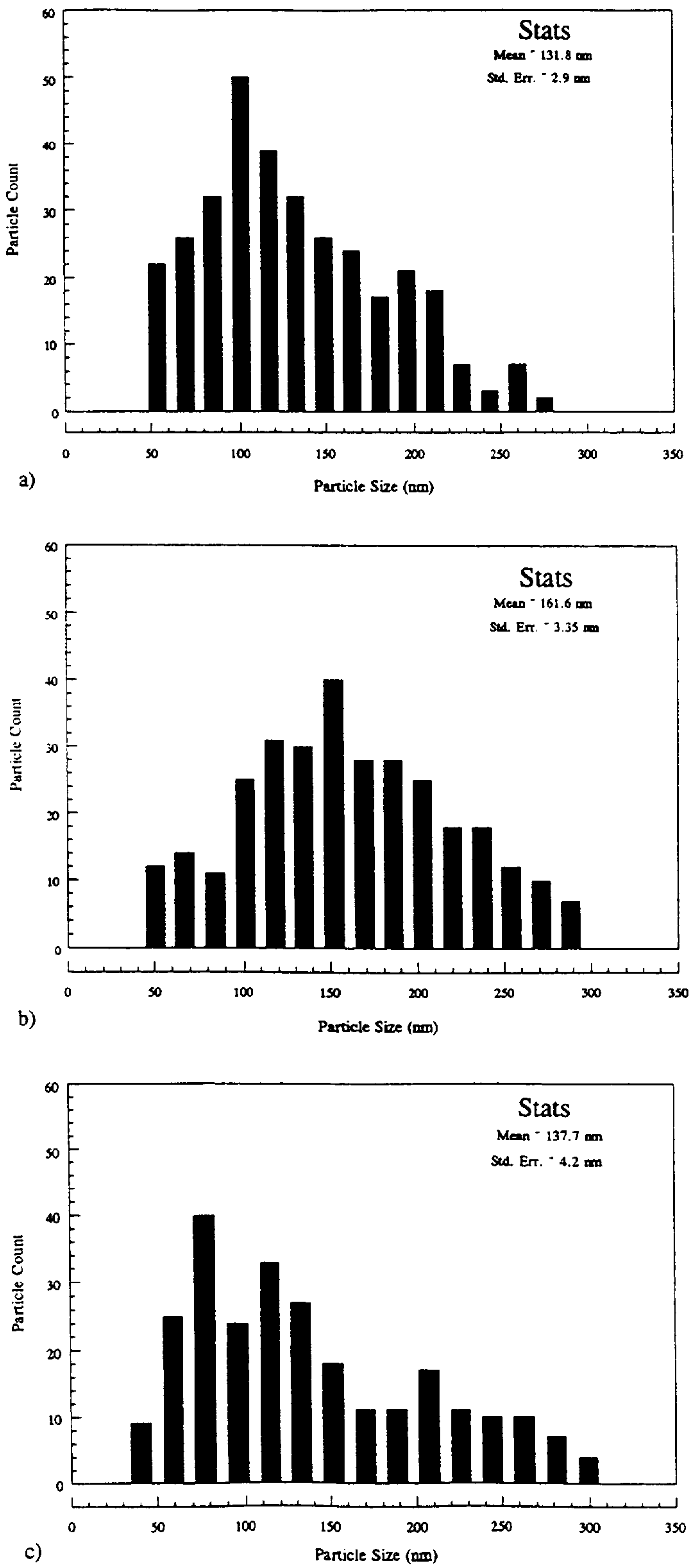

Figure 17 - Histograms of particle size distributions (PSDs) for small (secondary) precipitates after aging at 1173 K for a) 1 h; b) 10 h; and c) 100 h.

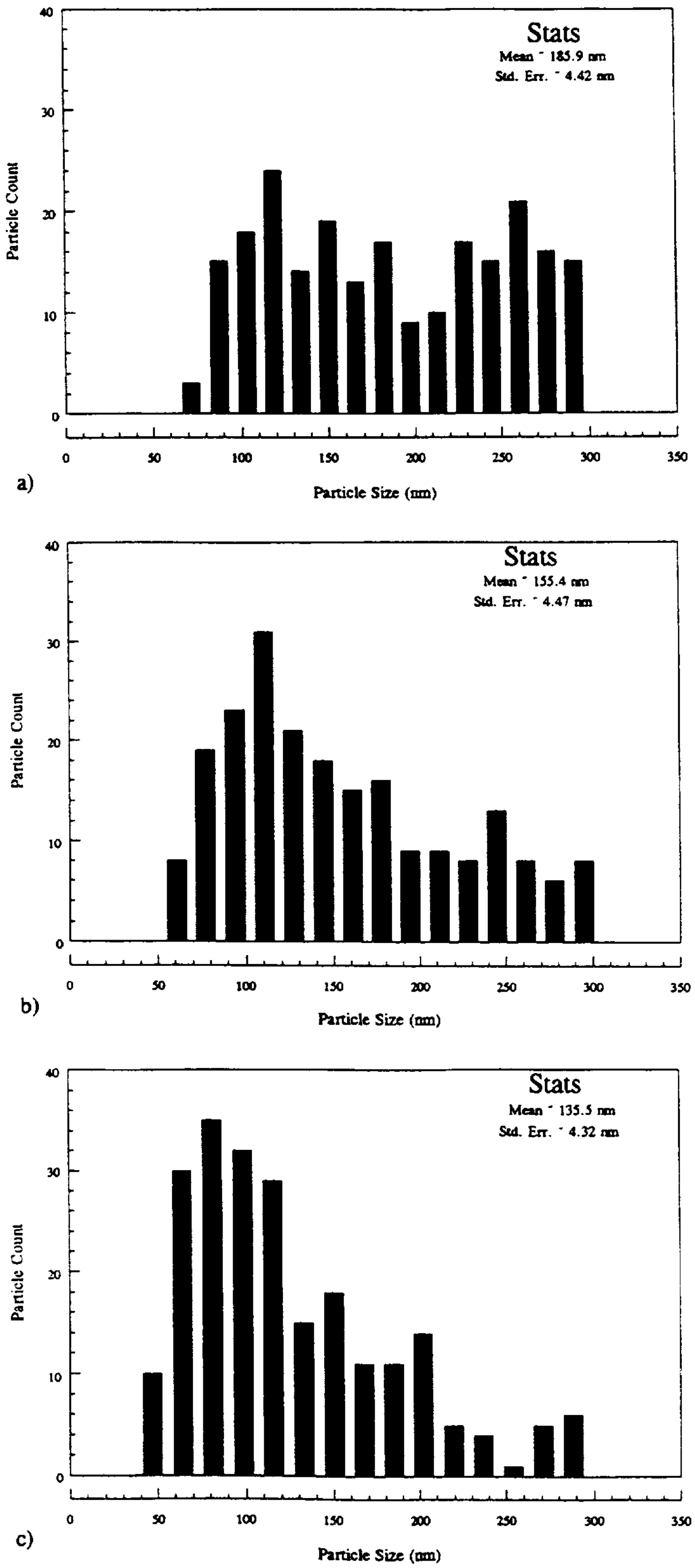

Figure 18 - Histograms of PSDs for small (secondary) precipitates after aging at 1323 K for a) 1 h; b) 10 h; and c) 50 h.

The particle-size histograms for large particles in the as-received powder and as-extruded bars are shown in Figure 19. The histograms of the primary particle size after annealing at 1323 K for 1 to 100 hours are shown in Figure 20, and the mean particle sizes are presented in Table II. Typical SEM micrographs showing relative particles sizes of primary particles aged at 1323 K are shown in Figure 21. The mean primary particle size gradually increases with annealing time as shown in Table II. Results from aging at 973 K presented in Table I show that in this temperature range the coarsening was not significantly affected by temperature.

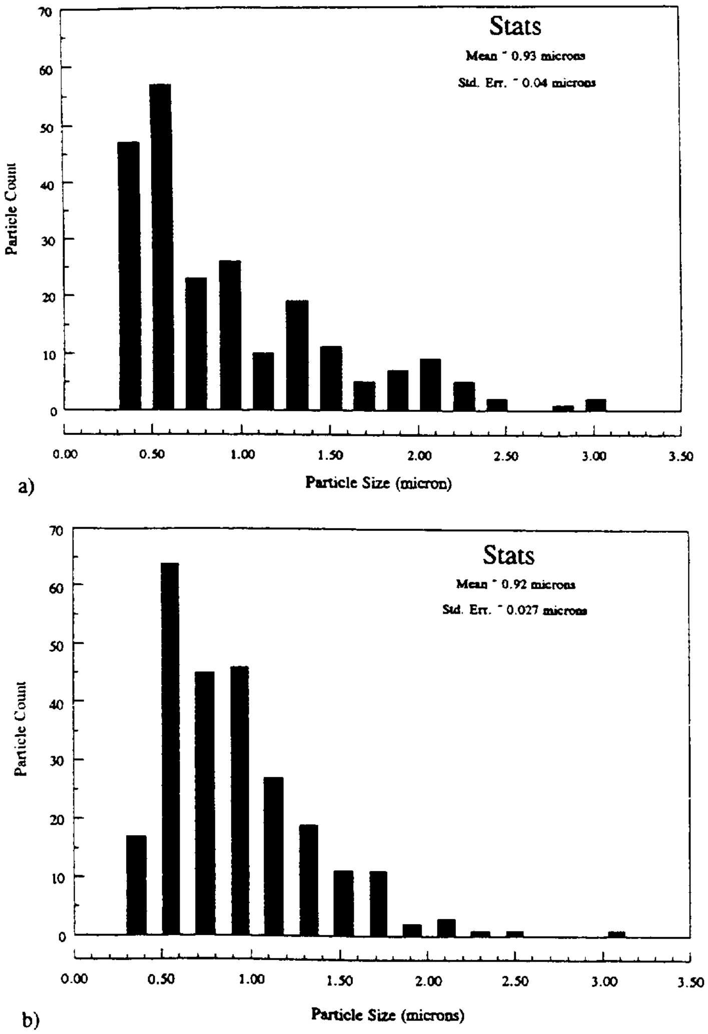

Figure 19 - Histograms of PSDs for large (primary) particles for a) As-atomized powders and b) As-extruded condition.

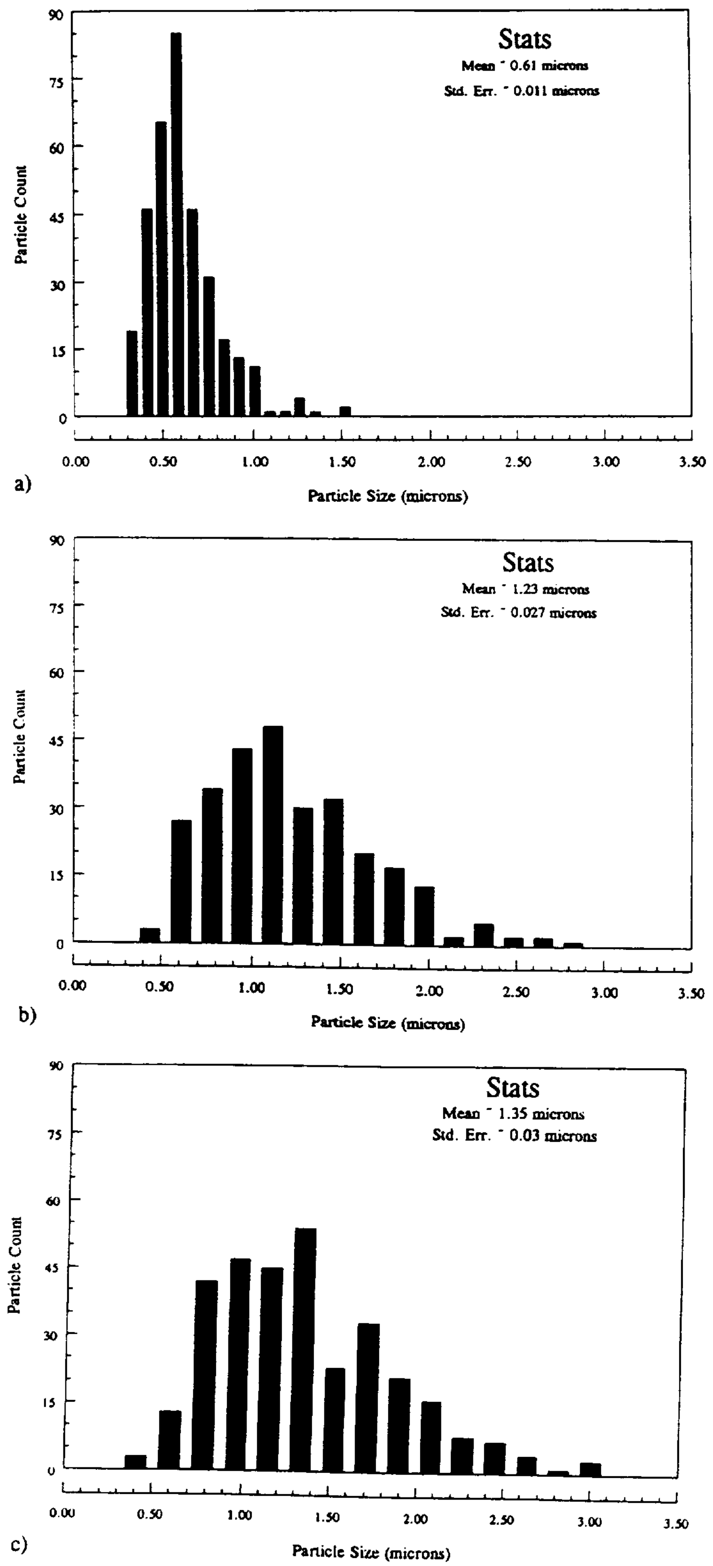

Figure 20 - Histograms of PSDs for large (primary) precipitates after aging at 1323 K for a) 1 h; b) 50 h; and c) 100 h.

Table II - Effect Of Aging On Primary Cr_2Nb Precipitate Mean Size

Aging Temperature (K)	Aging Time (h)	Mean Precipitate Diameter (μm)
As-Received Powder		0.93 ±0.04
As-Extruded		0.92 ±0.03
973	50	0.93 ±0.06
1323	1	0.61 ±0.01
1323	50	1.23 ±0.03
1323	100	1.35 ±0.03

Although some coarsening occurs when compared to as-atomized or as-extruded material, the average primary particle size after 100 h at 1323 K remains on the same order of magnitude. This result illustrates the sluggish coarsening process of the primary Cr_2Nb precipitates. Due to this slow coarsening of both the primary and secondary particles, a sufficient size difference between primary and secondary particles still exists even after prolonged exposures at very high temperatures. This current observation confirms a previous arbitrary experimental cut-off value of 300 nm that was considered for the difference between primary and secondary particles [5].

3.2.3 Matrix Grain Structure

The copper matrix displays an equiaxed grain structure in the plane transverse to the extrusion direction at all temperatures used in the present study (Fig. 22). Optical metallography of the bars in the longitudinal direction did indicate elongation of the copper grains in the extrusion direction. The aspect ratio of the grains in the longitudinal direction was ~4.0. The average grain size in the transverse direction was 1.6 μm after 10 h at 1173 and 2.7 μm after 100 h at 1323 K. The maximum value of grain size in the latter specimen was 4 μm. These values are comparable with an average grain size of 0.9 μm found previously for specimens aged up to 973 K [5]. Finally, Fig. 22 also reveals

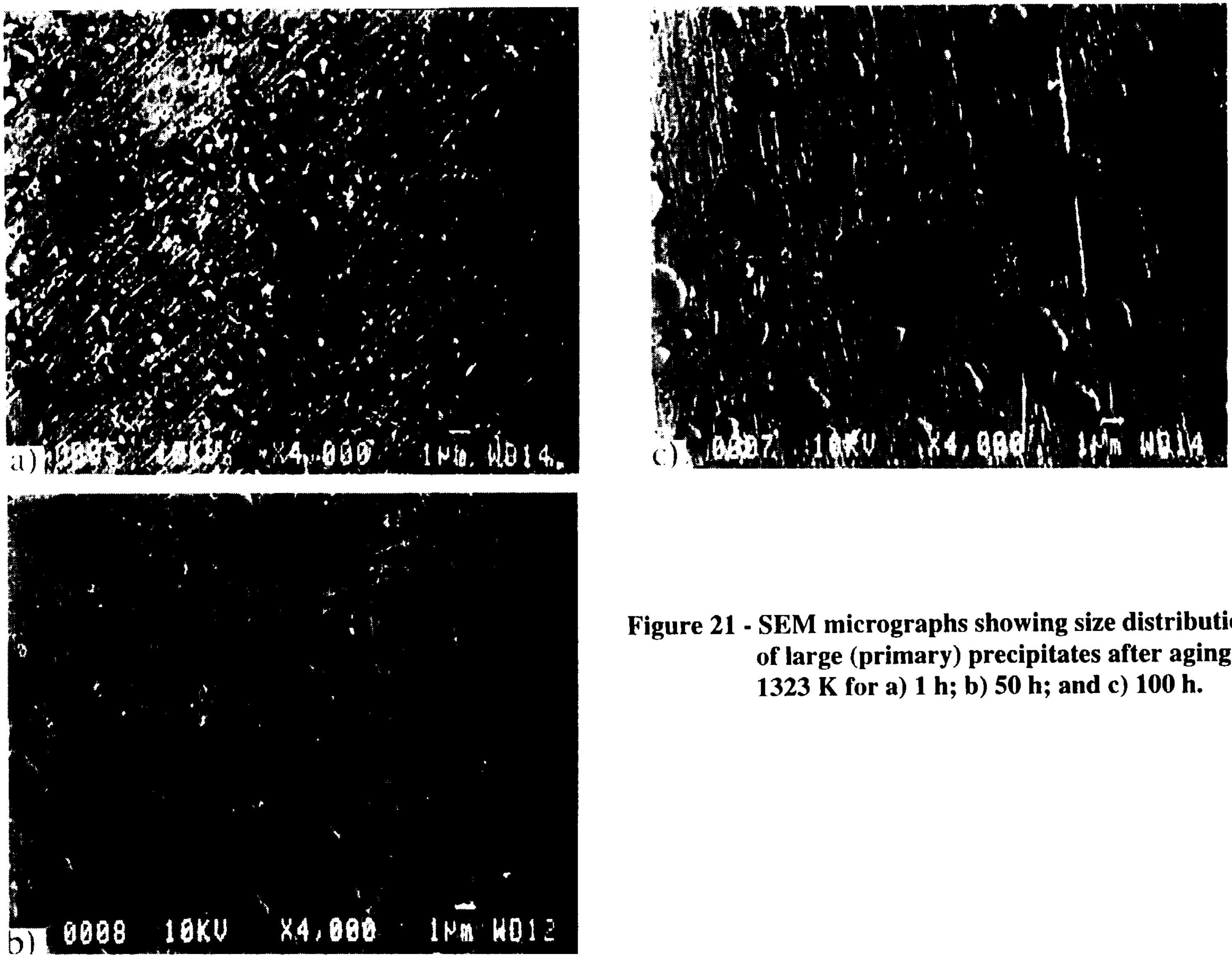

Figure 21 - SEM micrographs showing size distribution of large (primary) precipitates after aging at 1323 K for a) 1 h; b) 50 h; and c) 100 h.

primary and less frequently secondary particles residing at grain boundaries and triple points. These precipitates appear to provide effective grain-boundary pinning.

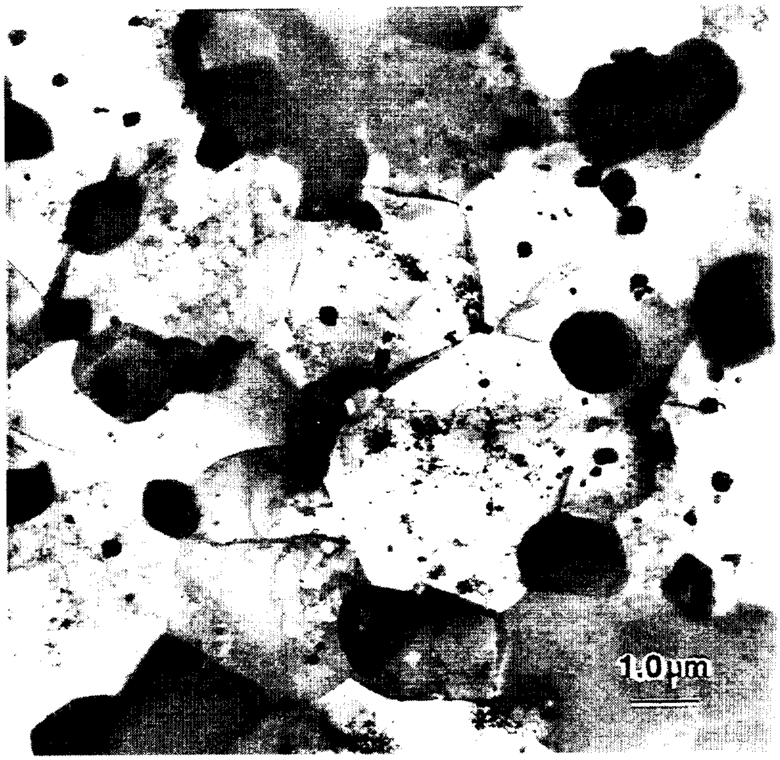

Figure 22 - Matrix grain structure in Cu-8 Cr-4 Nb alloy after aging at 1323 K - 100 h.

Finally, Fig. 23 shows the microhardness (HV) variation as a function of temperature for 100 hour anneal. Even after extensive high temperature exposure, e.g., after 100 h at 1323 K, the hardness reduces by only 38 HV from the as-extruded value of 128 HV. All these results indicate the good thermal stability of this alloy. Despite the decrease with aging temperature, the retained mechanical property values are notably superior to traditional alloys such as NARloy-Z.

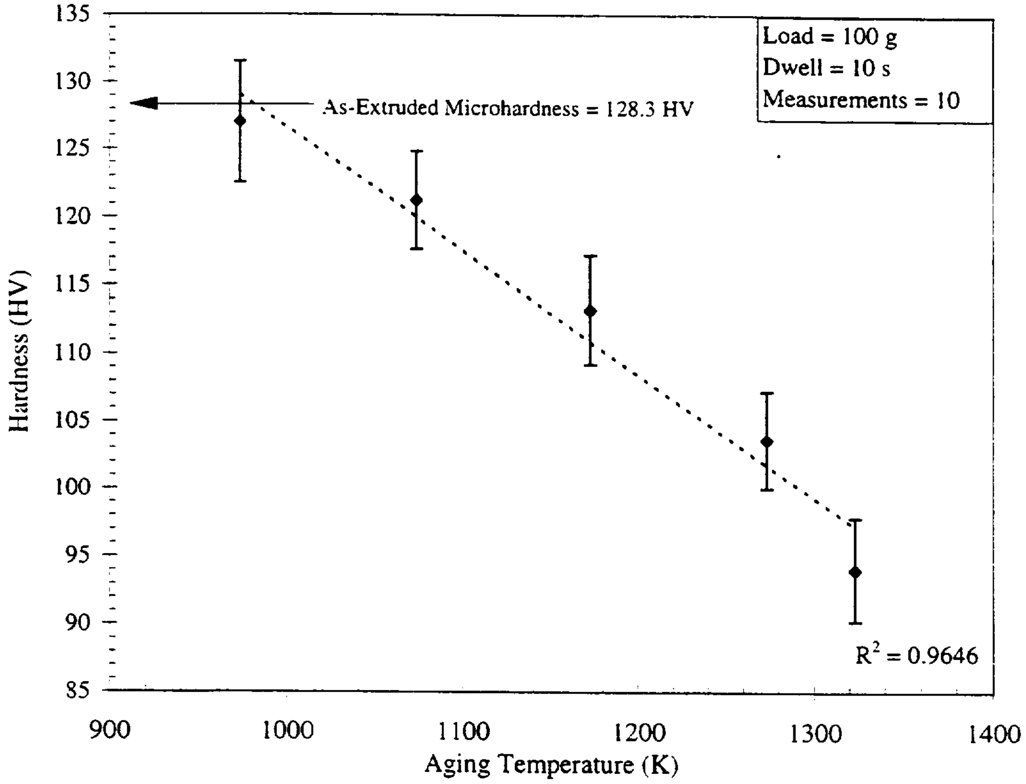

Figure 23 - Effect of Aging 100 h on room temperature microhardness (Vickers') of Cu-8 Cr-4 Nb alloy.

3.2.4 Oxygen Contamination

With the use of a LECO TC-136 Simultaneous N/O Determination Instrument the oxygen level of the consolidated alloy material studied was measured to be 1047 ppm. This relatively high level of oxygen contamination (compared to the nominal level of 260 ppm in the initial powder) most likely resulted from processing, e.g., vacuum not being high enough during encapsulation in steel cans, etc.

3.3 DISCUSSION

3.3.1 Cr_2Nb Precipitate Structure

As indicated by the pseudo-binary Cu-Cr_2Nb diagram(s) calculated by Michal [32] (see Fig. 24) and prior experimental observations [2], the Cr_2Nb phase precipitates directly out of the liquid at the hypereutectic composition of the present alloy. Consequently, many primary particles exhibit a complex, irregular shape, as observed in Fig. 14a. Previous research indicated that primary particles are formed during chill block melt spinning (CBMS) of a similar alloy [2]. In the melt spun material, the primary particle size was extremely small (tens of nm) due to the very high cooling rate (about 10^6 K/s). The present alloy was produced by gas atomization that involves significantly lower cooling rates (10^2-10^3 K/s) than CBMS. Therefore, the primary Cr_2Nb particles grew considerably larger (micron size, Fig. 2) in the atomized alloy as compared to the melt spun counterpart.

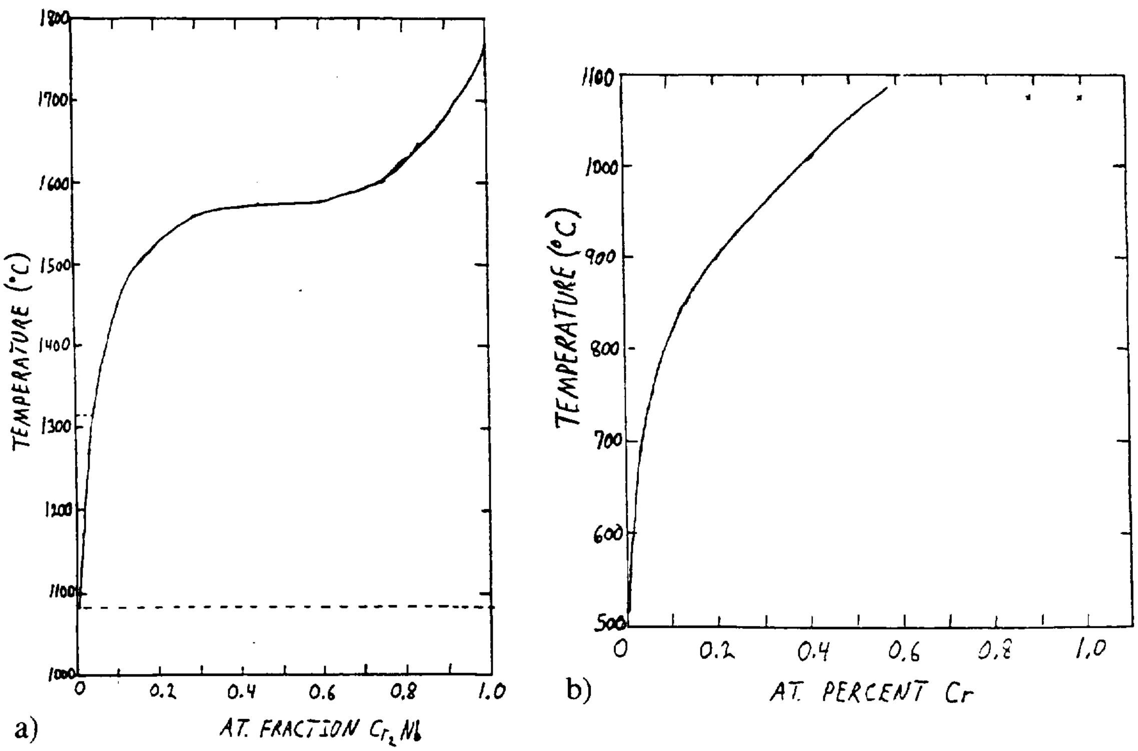

Figure 24 - a) Pseudo-binary Cu-Cr_2Nb phase diagram and b) Solid solubility (solvus) of Cr in Cu-Cr_2Nb, as calculated by Michal [32].

In contrast, the smaller secondary precipitates form from the supersaturated copper solid solution during cooling below the solvus temperature. The sizes of secondary Cr_2Nb precipitates were calculated considering an undercooling of about 100 K below the solidus and 773 K as the lower temperature bound for significant diffusion [33]. Briefly, this calculation was based on the available flux of atoms inside a sphere of radius $\sqrt{Dt}$ (D is diffusivity of the slowest moving species and t - cooling time between solidus and 773 K) that move to the center to form the Cr_2Nb precipitates having a particular (fcc) crystal structure [2]. Nb was considered to be rate limiting (controlling) specie since it has a lower diffusivity in Cu than does Cr, as expressions below directly indicate [34]:

$$D_{Cr} = 0.337\exp\left(-\frac{195{,}016\ \mathrm{J/mol}}{RT}\right)\mathrm{cm}^2/\mathrm{s}\ \text{and} \qquad (11a, b)$$

$$D_{Nb} = 2.04\exp\left(-\frac{251{,}291\ \mathrm{J/mol}}{RT}\right)\mathrm{cm}^2/\mathrm{s}.$$

For example, at 1323 K $D_{Cr} > 20D_{Nb}$, i.e. $6.73\mathrm{x}10^{-9}$ cm^2/s for Cr vs. $2.44\mathrm{x}10^{-10}$ cm^2/s for Nb.

Particle size calculations for cooling rates of 10^2-10^3 K/s, i.e. inert gas atomization, were performed for Cr, Nb and Cr_2Nb particles based on time-averaged diffusivities of Cr and Nb in Cu. Such average diffusivities were determined by methods put forth by Crank [35]. The following equation is a rendition of Crank's Eqn. (7.3) for time-incorporated diffusivity:

$$T_B = \int_0^t D_B(t')dt' = \int_0^t D_{o,B}\cdot\exp\left[\frac{Q_B}{R\cdot[T_o - c\cdot t']}\right]dt' \qquad (12)$$

where T_o = initial temperature (K) at onset of cooling (solidification);

c = cooling rate in K/s;

t = total time duration considered for cooling (s); and

t′ = time interval (s).

The average diffusivity is given by dividing the above integral by the total time, i.e.

$$\overline{D}_B = \frac{T_B}{t} \text{ cm}^2/\text{s}. \tag{13}$$

The combination of Eqns. (12) and (13) can be represented in the following summation form [2]:

$$\overline{D}_B = \frac{\sum_{\Delta t=0}^{n} D_B(t')\Delta t'}{\sum_{\Delta t=0}^{n} \Delta t'} \tag{14}$$

Actual calculations of $\overline{D}_{Cr}$ and $\overline{D}_{Nb}$, using Eqns. (11) and (14), and calculations of particle sizes based on these diffusivities are presented in Appendix 2. The results indicate that the size of the secondary Cr_2Nb particles formed from supersaturated solid solution upon solidification and subsequent cooling ranges between 16 and 50 nm. The calculated secondary particle size values seem in reasonable agreement with the previous assumption (based solely on microstructural features) that particles on the order of tens of nanometers are secondary particles. From the above calculation, it is also clear that the large particles around 1 μm could not form by precipitation from solid solution and therefore are primary particles. The combination of solidification and solid state precipitation processes gives the rapidly solidified powders an initial bimodal Cr_2Nb particle distribution with larger primary and smaller secondary particles, as can be seen in Fig. 14a.

The extrusion was performed at sufficiently high temperature (1133 K) to allow the small precipitates to dissolve back into copper solid solution. According to the Cu-Cr_2Nb phase diagram, these alloying elements show substantial solubility at temperatures above 1100 K [32]. The cooling rate after extrusion was also sufficiently fast to maintain a supersaturated copper solid solution. In fact, a subsequent precipitation of particles from this supersaturated solid solution has been demonstrated [5]. For example, aging at temperatures below the solvus (773 and 973 K) gives rise to a normal precipitation behavior with nucleation and growth of new secondary particles giving subsequent strengthening after short holding times (e.g., 1 hr at 773 K, which gives an average size of ~30nm). As already mentioned, this precipitation process explains the typical bimodal particle microstructure observed in aged materials.

At temperatures comparable to or higher than the extrusion temperature, processes more complex than precipitate nucleation and growth take place. While still limited at very high temperatures, such as 1323 K, Ostwald ripening of larger secondary particles leads to their growth (in the order of hundreds of nanometers, but with most remaining in the *secondary* size category) at the expense of smaller ones, which dissolve. At the same time, since 1323 K is well above the solvus line, these smaller precipitates also shrink due to going back into solution. Upon furnace cooling from 1323 K, a new generation of very fine secondary Cr_2Nb particles (in the range of tens of nanometers) precipitate out of this supersaturated solid solution, resulting in a trimodal particle distribution as seen in Fig. 14c.

Some of the newly precipitated particles were identified as NbO. The NbO probably forms as Cr rapidly diffuses away from the dissolving Cr_2Nb precipitates leaving a Nb rich region. Oxygen from the matrix, likely introduced during powder handling, can then readily react at these temperatures to form the NbO. This mechanism becomes more prevalent at higher temperatures with NbO accounting for as much as 30% of the fine precipitates at 1173 K.

3.3.2 High Temperature Cr_2Nb Stability/Coarsening Behavior

The coarsening data for primary particles at 1323 K were analyzed to determine the governing process assuming no real change in volume fraction occurs. Since primary particles form from liquid and only limited dissolution has been observed, the assumption that the volume fraction remains roughly constant seems reasonable. Previous measurements of large particle volume fractions after aging at 973 K seemed to confirm this assumption [5]. Figure 25 shows a plot of $\bar{r}^2$, $\bar{r}^3$, and $\bar{r}^4$ versus time, where $\bar{r}$ is the average radius of the precipitates. A linear relationship was assumed, and a straight line was fit to the data using a least squares linear regression. The data fit both volume and grain-boundary diffusion controlled (VDC and GBDC) coarsening kinetics. The grain boundary ripening is in accordance with the preferred distribution of the large precipitates at grain boundaries and/or triple points (e.g., Fig. 14b and Fig. 22). A comparison of the experimental value of the coarsening rate constant ($k=5.6 \times 10^{-31}$ m^4/s) with a calculated value for GBDC, i.e. evaluation of Eqn. (7) is not possible since no grain boundary diffusion data are available for the present system.

The plot of Fig. 25 was further analyzed for the slopes of the $\bar{r}^3$ and $\bar{r}^4$ fitted lines. The slope of the $\bar{r}^3$ line, i.e. the VDC LSW rate constant, k, was calculated to be roughly ~7.78×10^{-25} m^3/s while that for the GBDC case was ~5.6×10^{-31} m^4/s. These are reasonable values compared to those determined for other DS systems, e.g., ref [10]. A k value of the VDC case of unmodified LSW was also calculated based purely on material parameters for comparison with the experimentally determined k. Nb was considered the rate-controlling species since it has lower diffusivity in Cu than Cr, as pointed out earlier. Using Eqn. (5), considering a temperature of 1323 K, at which $D_{Nb} \approx 2.44\times10^{-14}$ m^2/s and $C_{Nb} \approx 0.001$ [4a], and taking $V_m \approx 2.58\times10^{-5}$ m^3/mol and $\gamma \approx 0.5$ J/m^2, typical for incoherent precipitates, gave $k \approx 2.54\times10^{-26}$ m^3/s, which is reasonably close to experimental value (by about an order of magnitude). These relatively low values of diffusivity and solubility of Nb in Cu help explain the apparent sluggish coarsening of the large precipitates, as mentioned earlier.

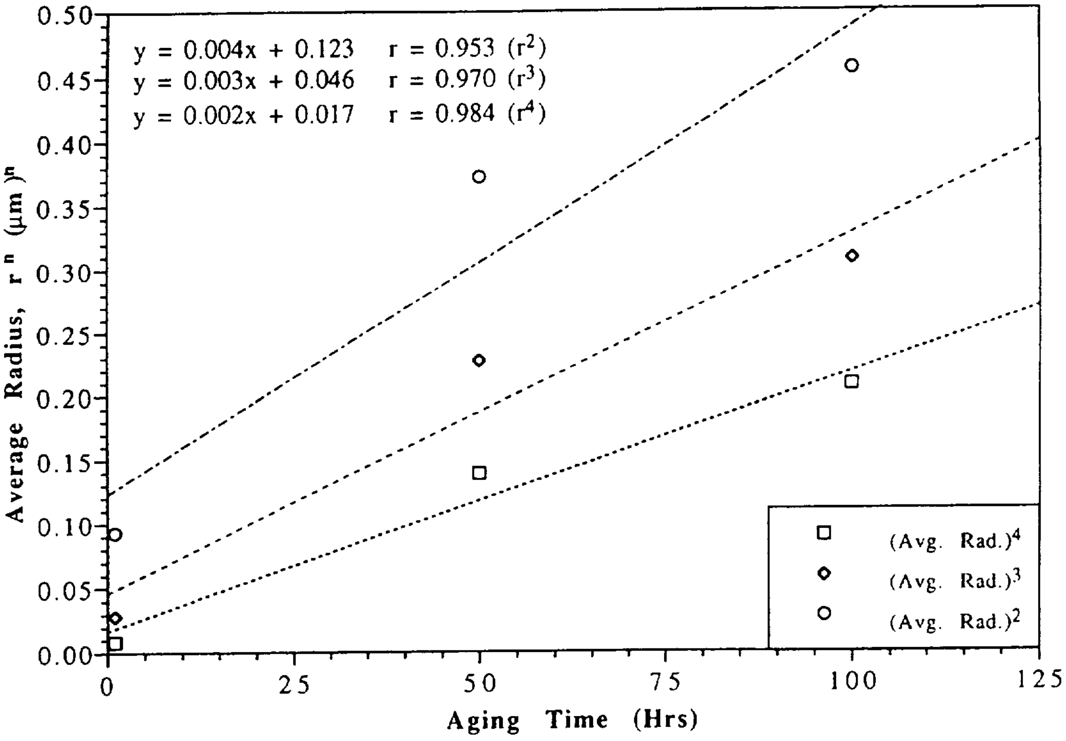

Figure 25 - Average Large Cr_2Nb Particle Radius, $\bar{r}$, Vs. Aging Time at 1323 K for Cu-8 Cr-4 Nb alloy. (Plot of $\bar{r}$ raised to power 2, 3, and 4 where slopes give corresponding rate constants, k, for possible rate controlling processes: interface controlled, volume diffusion controlled, and grain boundary controlled, respectively.)

A detailed analysis of grain-boundary diffusivity (of Nb in Cu), D_{gb}, solubility of Nb in the grain boundary, $C_{e,\infty,gb}$, fraction of grain boundaries covered by dispersoids, f, and grain boundary thickness, δ, has not been undertaken as of yet. Therefore, a rigorous calculation of the rate constant, k', for GBDC coarsening (Eqn. (6)) and subsequent comparison with experimental value cannot be completed. But, again, the best fit curve for $\bar{r}^4$ in Fig. 25 evidently points to this type of coarsening behavior (mechanism). Finally, Premkumar, *et al.* [10] also show that their experimental and calculated coarsening data for $FeNiAl_9$ precipitates in aluminum best fit the GBDC model - Eqn. (6). They also discovered that the majority of such particles do indeed primarily inhabit grain boundaries.

Modifications of the coarsening kinetics given by LSW theory for such effects as non-steady state processes and finite volume fractions give kinetics factor variations of 1 to ~5, depending on particular modification (e.g., refer to Fig. 12). For instance, an increase in particle volume fraction from 0.19 to 0.32 caused only doubling of the coarsening rate constant [10]. The one order of magnitude difference points to a real increase in the coarsening kinetics that is likely caused by faster grain boundary diffusion. It appears most probable that Ostwald ripening with both bulk and grain boundary diffusion is the mechanism operating to coarsen the Cr_2Nb precipitates. This is supported to some extent by the fact that some primary precipitates do exist within grains (e.g., Fig. 14a), although a majority are at grain boundaries. In addition, secondary particles, found mostly inside grains (e.g., Fig. 14c and Fig. 22), may also contribute to primary particle coarsening. But GBDC coarsening mechanism most likely dominates (at least for primary precipitates), which, again, is supported by the large precipitate morphology (primarily at grain boundaries) revealed in Figs. 14b and 22.

In contrast to aging below 1200 K, the secondary particles show a continuous decrease in average size during aging at 1323 K as shown in Fig. 18. As alluded to earlier, this is most likely due to the additional dissolution of particles back into the matrix when the aging temperature puts the alloy above the solvus line of the pseudo-binary Cu-Cr_2Nb phase diagram [32]. The experimental observation of a solvus line between 1200 and 1323 K is in agreement with the solvus line calculation by Michal. Thus, the smallest secondary precipitates not only dissolve due to larger ones coarsening, but also shrink by being thermodynamically driven back into solution. Finally, since these particles actually exhibit a decrease in average size they, of course, cannot follow or be modeled by an LSW-type growth-rate theory.

Despite this evident dissolution of smaller secondary precipitates, they remain in sufficient number even at these extremely high aging temperatures to provide significant room temperature strengthening. At 1323 K, new secondary precipitates form during subsequent cooling as shown in Figure 14c. In addition, Cr-and Nb-rich particles also form and have sizes comparable to the secondary particles. Compared to secondary precipitates, larger primary particles are less thermodynamically affected, i.e. more stable, due to much lower capillarity effects or reduced overall specific surface area (energy). Therefore, primary precipitates exhibit slow net coarsening (coarsening exceeding any resolution) that becomes evident at temperatures above 1000K.

Finally, the experimentally observed stability of mechanical strength of Cu-8 Cr-4 Nb alloys even after being exposed to temperatures very close to their melting point is revealed in Fig. 23. This is clearly related to and evidence of the sluggish coarsening of the dispersed Cr_2Nb phase and, ultimately, the grains, which will be touched on further shortly.

3.3.3 Cr-Rich and Nb-Rich Particle Precipitation/Formation

Cr_2Nb was not the only particle to precipitate out (form) during high-temperature exposure. Niobium-rich (NbO) and Cr-rich particles were also detected (via TEM observation and confirmed by EDS and electron microdiffraction [31]). As already described, resolution of the Cr_2Nb precipitates presumably occurs simultaneously with coarsening/dissolving at temperatures greater than 1100 K. First, large precipitates grow at the expense of the small(est) dissolving particles, which obviously necessitates diffusion of solutes. Second, small precipitates are driven back into solid solution above the solvus line. This conventional coarsening picture is complicated in Cu-Cr-Nb alloys by the presence of two solutes. Moreover, the diffusivities of the two components are significantly different [34, 36]. Cr diffuses over one order of magnitude faster than Cu, whereas Nb diffuses slower than Cu. When Cr_2Nb precipitates dissolve both Cr and Nb must diffuse through the copper matrix to reach growing larger precipitates. Such a coarsening process of the Cr_2Nb precipitates was experimentally observed in the present Cu-8 Cr-4 Nb alloys. Finally, the coarsening behavior is complicated by the presence of such Nb-rich and Cr-rich precipitates.

A simplistic explanation based on the Gibbs phase rule indicates this ternary alloy should feature a maximum of three phases at non-critical temperatures (when the temperature may be one of the independent variables). The present alloy contains four phases which again suggests that Cr-rich and Nb-rich phases are out of equilibrium. But if oxygen (extraneous, or unintentional oxygen introduced during processing) is taken as the fourth component the total number of equilibrium phases will become four. Phase identification revealed that Nb atoms evidently react with oxygen to form NbO. Table III gives a comparison of the relative Gibbs free energy of formation (ΔG_f) for possible Cr and Nb compounds/phases for the temperature range of 1000-1300 K.

Table III: Heat of Formation and Crystal Structure of Possible Phases

Compound/ Phase	ΔG_f (kJ/mol)	Crystal Structure
Cr	- -	cubic, bcc
Nb	- -	cubic, bcc
Cr_2Nb	-23	cubic, fcc (C15)
Cr_2O_3	-830	rhombohedral
NbO	-320	cubic
NbO_2	-580	tetragonal
α-Nb_2O_5	-1400	monoclinic
Ref.	[37]	[38]

An interesting point is that the least stable oxide, NbO, is formed instead of Nb_2O_5, which is thermodynamically favored. An explanation could lie in the difference in their crystal structures (Table III), which could dictate a preferred nucleation orientation. In other words, the NbO phase is presumably kinetically favorable since it has simplest crystal structure. Nb0 is cubic with **a** ≈ 0.421nm, whereas α-Nb_2O_5 is monoclinic, with **a** and **c** ≈ 2.0nm and NbO_2 is tetragonal with **a** and **c** ≈ 1.37nm and ≈ 0.6nm, respectively [38]. Copper is of course fcc with **a** ≈ 0.3615nm.

The above anomalous, unexpected "non-equilibrium" phases require further investigation into reasons for their existence. The investigation/explanation should consider the driving force for Cr-rich and NbO phase formation as well as kinetic considerations based on particle structure, orientation relationships and component diffusivities.

3.3.4 Grain-Boundary Pinning

Finally, the effect of particle coarsening on grain size is touched on. It has been shown [39] that comparison of the calculated strengthening effects (i.e. Orowan and grain boundary) upon aging at 1323 K and 973 K indicates that the predominant contribution in both cases is due to grain boundary strengthening. This is supported by the essentially same micrometer grain size range that was experimentally observed even after 100 hr at 1323 K [39]. This clearly demonstrates the pinning effect of the precipitates, which does not markedly diminish when they grow in the size range encountered in these alloys. Calculations of the maximum grain size according to the Hillert-Gladman [40, 41] expression,

$$d_{calc} = \frac{4r}{3f} \tag{15}$$

where r is particle radius and f volume fraction, were made to further distinguish between the pinning effect of small versus large particles. The calculated grain size of 4.2 μm considering small particles was in better agreement with the observed values of 4 μm than the calculated value of ~8 μm for the larger (primary) particles. This suggests that secondary particles are more effective at pinning the grain boundaries than are the primary particles. This, of course, is contrary to expectation since primary precipitates are almost entirely found at grain boundaries as opposed to secondary particles. An explanation for this anomaly may lie in experimental error, e.g., initial volume fraction measurements, and requires further investigation.

4. SUMMARY AND CONCLUSIONS

- Cu-8 Cr-4 Nb alloys exhibit a bimodal distribution of Cr_2Nb particles, namely, primary micrometer range particles formed from liquid and secondary particles formed by precipitation from solid solution. A trimodal particle distribution with additional very fine secondary particles is observed after slow cooling from temperatures above the extrusion temperature.

- The copper matrix exhibits a fine equiaxed structure with an average grain size of 2.7 μm after exposure at 1323 K after 100 h. No significant grain growth occurs in the studied temperature range. This is most likely due to effective grain boundary pinning by Cr_2Nb particles.

- The coarsening process of Cr_2Nb particles is very slow; both primary and secondary precipitates remain in the same size range after high temperature exposure up to 1323 K for 100 h. This can be attributed to low solubility and diffusivity of Nb in Cu.

- Coarsening kinetics of primary precipitates are consistent with either volume or grain boundary diffusion mechanisms; but most likely mainly grain-boundary diffusion controlled, since large particles are usually found at grain boundaries.

- The LSW theory explains primary Cr_2Nb precipitate coarsening behavior.

- Neither of the LSW coarsening kinetic equations take into account the case of a 'mixing' or simultaneous occurrence of diffusion controlled and interface reaction controlled ripening.

- Modifications to LSW theory have been formulated to take into account finite volume fraction and elastic strain effects of particles. This along with the previous statement could explain deviation of experimental data from LSW theory. The modified theories usually give better experimental fit.

5. REFERENCES

1. D. L. Ellis and R. L. Dreshfield, "Preliminary Evaluation of a Powder Metal Copper - 8 Cr- 4 Nb Alloy" presented at 1992 Conference on Advanced Earth-to-Orbit Propulsion Technology, May 19-21, 1992, Marshall Space Flight Center, Alabama.

2. D. L. Ellis, "Precipitation Strengthened High Strength, High Conductivity Cu-Cr-Nb Alloys Produced by Chill Block Melt Spinning", PhD Thesis, Case Western Reserve University, Cleveland, Ohio, August 1989. See also NASA CR 185144, NASA Lewis Research Center, Cleveland, Ohio, Sept. (1989).

3. D.L. Ellis, A.K. Misra and R.L. Dreshfield, "Effect of Hydrogen on a Cu-8 Cr-4 Nb Alloy," NASA TM-106429, NASA Lewis Research Center, Cleveland, OH (Dec. 1993).

4. a) D. J. Chakrabati and D. E. Laughlin, *Bull. Alloy Phase Diagrams*, **2**, 1982, p. 507 and **5**, 1984, p. 59, 99.
   b) D. J. Thoma and J. H. Perepezko, *Mat. Sci. Eng.*, **A156**, 1992, 97.

5. K. R. Anderson, J. R. Groza, R. L. Dreshfield and D. L. Ellis, *Mat. Sci. Eng.*, **A169**, 1993, 167.

6. D. L. Ellis, R. L. Dreshfield, M. J. Verrilli, and D. G. Ulmer, "Mechanical Properties of a Cu-8 Cr- 4 Nb Alloy," Advanced Earth-to-Orbit Propulsion Technology Conference, NASA Marshall Space Flight Center, Huntsville, Alabama, May 17-19, 1994.

7. J. J. Stephens and C. R. Hills. "Long Term Stability of Two Dispersion Strengthened Copper Alloys at Elevated Temperatures," Sandia National Laboratories, Albuquerque, New Mexico, 1990.

8. D. A. Porter and K. E. Easterling, <u>Phase Transformations in Metals and Alloys</u>, Chapman and Hall, London, 1990.

9. M. Hillert, <u>Lectures on the Theory of Phase Transformations</u>, Ed. by H. I. Aaronson, American Institute of Mining, Metallurgical and Petroleum Engineering, Inc., New York, 1986, p. 26.

10. M. K. Premkumar, A. Lawley, and M. J. Koczak, *Metall. Trans.*, **23A**, 1992, 3219.

11. G. J. Shiflet and J. A. Hawk, <u>Dispersion Strengthened Aluminum Alloys</u>, Ed. Y.-W. Kim and W. M. Griffith, The Minerals, Metals & Materials Society, 1988, p. 123.

12. P.W. Voohees and M.E. Glicksman, *Metall. Trans.*, **15A**, 1984, 1081.

13. I. M. Lifshitz and V. V. Slyozov, *J. Phys. Chem. Solids*, **19**, 1961, 35.

14. C. Wagner, *Z. Electochem.*, **65**, 1961, 581.

15. S. S. Kang and D. N. Yoon, *Met. Trans.*, **13A**, 1982, 1405.

16. *Idem. ibid.*, **12A**, 1981, 65.

17. Y. Seno, Y. Tomokiyo, K. Oki, and T. Eguchi, *Trans. Jpn. Inst. Metals*, **24**, 1983, 491.

18. T. Eguchi, Y. Tomokiyo, K. Oki, and Y. Seno, *Mat. Res. Soc. Symp. Proc.*, 1984, 475.

19. R. Watanabe and Y. Masuda, *Modern Devel. Powder. Metall.*, **6**, 1974, 1.

20. R. Watanabe, K. Tada, and Y. Masuda, *Z. Metallkde*, **13**, 1976, 619.

21. J.W. Martin and R. D. Doherty, Stability of Microstructure in Metallic Systems, Cambridge University Press, Cambridge, United Kingdom, 1976, pp. 173-93.

22. P. K. Footner and C. B. Alcock, *Metall. Trans.*, **3A**, 1972, 2633.

23. A. J. Ardell, *Acta. Metall.*, **20**, 1972, 61.

24. C. S. Jayanth and P. Nash, *J. Mat. Sci.*, **24**, 1989, 3041.

25. C. K. L. Davies, P. Nash, and R. N. Stevens, *Acta Metall.*, **28**, 1980, 179.

26. A. D. Brailsford and P. Wynblatt, *Acta Metall.*, **27**, 1979, 489.

27. J. D. Eshelby, *Acta Metall.*, **14**, 1966, 1306.

28. W. C. Johnson and P. W. Voorhees, *Metall. Trans.*, **16A**, 1985, 337.

29. D. J. Thoma and J. H. Perepezko, *Mat. Res. Soc. Symp. Proc.*, **194**, 1990, 105.

30. M. Takeyama and C. T. Liu, *Mat. Sci. Eng.*, **A132**, 1991, 61.

31. A. Garg, NASA Lewis Research Center, Private Communication, October 1993.

32. G. M. Michal, Case Western Reserve University, Private communication, 1993.

33. J. R. Groza, "Microstructural Features of A New Precipitation Strengthened Cu-8Cr-4Nb Alloy," *Mater. Charact.*, **31**, 1993, 133.

34. D. B. Butrymowicz, J. R. Manning, and M. E. Read, *Diffusion Rate Data and Mass Transport Phenomena for Copper Systems*, Diffusion in Metals Data Center, Metallurgy Division, Institute for Materials Research, National Bureau of Standards, Washington, D.C., (July 1977).

35. J. Crank, "*The Mathematics of Diffusion*," 2nd Ed., Clarendon Press, Oxford, 1975, p 104-105.

36. A. Almazouzi, M.-P. Macht, V. Naundorf, G. Neumann and V. Tolle, *Defect and Diffusion Forum*, **95-98**, 1993, 703.

37. I. Barin, *Thermochemical Data of Pure Substances*, VCH Verlagsgesellschaft mbH, Weinhein, 1993, p. 431, 1027-1029.

38. H. Nowotny and K. Seifert, *Atomic Energy Review, Part III*, International Atomic Energy Agency, Vienna, 1968.

39. K. R. Anderson, J. R. Groza, R. L. Dreshfield and D. L. Ellis, *Met. Trans.*, **26A**, 1995, 2197.

40. M. Hillert, *Acta Met.* **13**, 1965, 227.

41. T. Gladman, *Proc. Roy. Soc.*, **A294**, 1966, 298.

APPENDIX 1

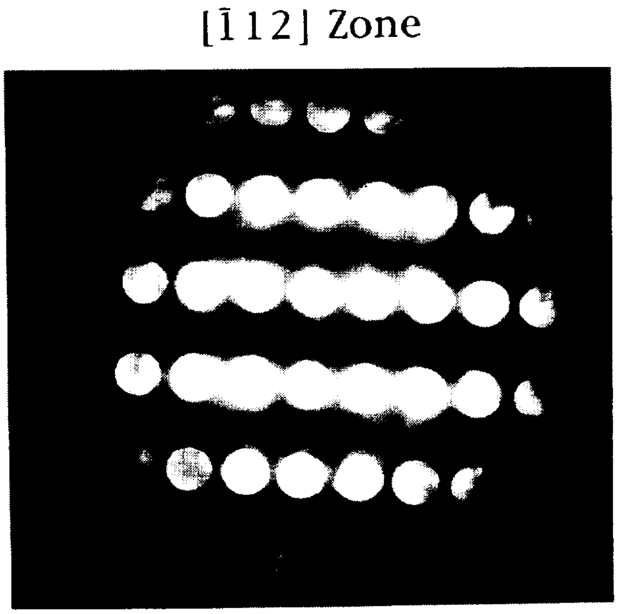

Figure A1 - **Convergent Beam Electron Diffraction (CBED) Pattern of fcc cubic secondary Cr_2Nb particle in Cu-8 Cr-4 Nb after aging at 973 K - 100 h.**

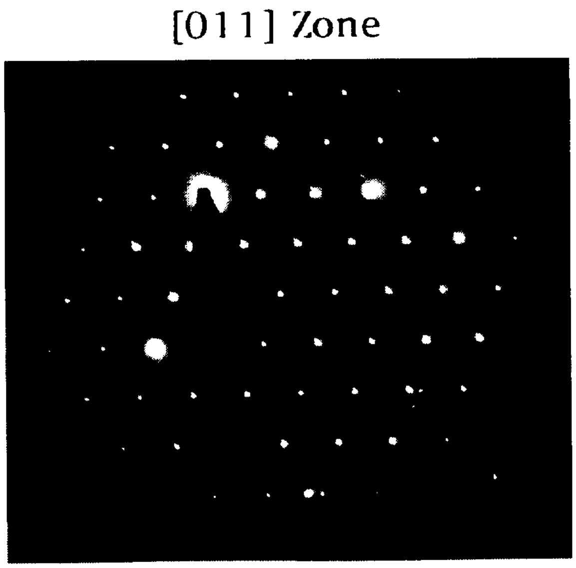

Figure A2 - **Selected Area Diffraction (SAD) Pattern identifying primary Cr_2Nb precipcipitate phase as fcc cubic in Cu-8 Cr-4 Nb after aging at 1323 K - 100 h.**

Appendix 2A: Size Calculations of Particles Formed During Gas Atomization (Solidification/Cooling) Process

The following assumptions are made about the inert gas atomization process:

1. Solidification initiates at a temperature 100 K below the melting point of Cu or 1256 K.
2. The cooling rate is 100 - 1000 K/s and is linear throughout the time of interest.
3. No significant diffusion occurs below 773 K.

Expressions for D_{Cr} and D_{Nb} are given again below:

$$D_{Cr} = 0.337\exp\left(-\frac{195{,}016\ \mathrm{J/mol}}{RT}\right)\mathrm{cm^2/s} \qquad \text{(A1)}$$

$$D_{Nb} = 2.04\exp\left(-\frac{251{,}291\ \mathrm{J/mol}}{RT}\right)\mathrm{cm^2/s} \qquad \text{(A2)}$$

The following formula, based on Crank's derivation (text Eqn. (14)), was used to estimate the average diffusivities:

$$\overline{D}_B = \frac{\sum_{\Delta t=0}^{n} D_B(t')\Delta t'}{\sum_{\Delta t=0}^{n} \Delta t'} \qquad \text{(A3)}$$

$\Delta t'$ is the time increment, dependent on number of steps/intervals, n; $T_o = 1256$ K; $T_f = 773$ K $\therefore\ \Delta T = 483$ K.

After numerically integrating the numerator of Eqn. (A3) and dividing by the total times (done on spreadsheet, Appendix 2b), the following diffusivities are obtained:

$D_{Avg.Cr} = 3.3\times10^{-10}$ cm^2/s and $D_{Avg.Nb} = 7.3\times10^{-12}$ cm^2/s

The assumption is made that half the atoms in a sphere with a radius equal to the square root of the average diffusivity times the total time diffuse to the center of the sphere and form the precipitate. It is also assumed that the concentration of Cr and Nb at the precipitate/matrix interface is zero.

Cooling Rate of c = $1x10^2$-$1x10^3$ is range for Ar gas atomization. The following calculations would be the same regardless of cooling rate; a cooling rate of c = 100 K/s is used for this case:

$$R_{Cr} = \sqrt{D_{Cr} \cdot 4.83\ s} = \sqrt{3.3x10^{-10}\ cm^2/s \cdot 4.83\ s} = 4.0 \times 10^{-5}\ cm = 400\ nm$$

$$R_{Nb} = \sqrt{D_{Nb} \cdot 4.83\ s} = \sqrt{7.3x10^{-12}\ cm^2/s \cdot 4.83\ s} = 5.94 \times 10^{-6}\ cm = 59.4\ nm.$$

The total volume of the spheres are determined using the above radii:

$$V_{Cr} = \frac{4}{3}\pi R_{Cr}^3 = \frac{4}{3}\pi(400\ nm)^3 = 2.68 \times 10^8\ nm^3$$

$$V_{Nb} = \frac{4}{3}\pi R_{Nb}^3 = \frac{4}{3}\pi(59.4\ nm)^3 = 8.77 \times 10^5\ nm^3$$

In order to calculate the total flux of atoms to the precipitate, it is necessary to determine the concentration of atoms per cubic nanometer.

The composition, in atomic percent (a/o), Cu-8 Cr-4 Nb, is considered in estimating atom fluxes. (It is assumed that a change in the Cu lattice parameter is effectively inconsequential.) By calculating the number of atoms of Cu per cubic nanometer and applying the respective a/o, the number of Cr and Nb atoms per cubic nanometer is determined.

Cu unit cell size calculation:

$a_o = 0.36153\ nm \Rightarrow$

$$V_{Cu} = a_o^3 = 0.047253\ nm^3$$

The number of Cr and Nb atoms in the appropriate sphere size just determined are calculated by calculating the number of Cu unit cells in the sphere volume and by multiplying by 4 Cu atoms per unit cell and atomic fractions of Cr and Nb, respectively.

$N_{Cr} = \#\ Cu\ unit\ cells \times 4 \times 0.08 \times 0.5$ First, for the number of Cu unit cells and atoms:

$$\#\text{ of Cu unit cells} = \frac{V_{Cr}}{V_{Cu}} = \frac{2.68\times10^{8}\text{ nm}^{3}}{0.047253\text{ nm}^{3}} = 5.673\times10^{9}\text{ unit cells}$$

$$\Rightarrow 5.673\times10^{9}\text{ unit cells}\times\frac{4\text{ atoms}}{\text{unit cell}} = 2.27\times10^{10}\text{ Cu atoms}$$

$$\Rightarrow N_{Cr} = 2.27\times10^{10}\times0.08\times0.5 = \mathbf{9.08\times10^{8}\ Cr\ atoms.}$$

$$N_{Nb} = \#\text{ Cu unit cells}\times4\times0.08\times0.5 = \frac{V_{Nb}}{V_{Cu}}\times4\times0.08\times0.5$$

$$\Rightarrow N_{Nb} = \frac{8.77\times10^{5}\text{ nm}^{3}}{0.047253\text{ nm}^{3}}\times\frac{4\text{ Cu atoms}}{\text{unit cell}}\times0.04\times0.5 = \mathbf{1.485x10^{6}\ Nb\ atoms.}$$

<u>Size of (possible) Cr Precipitates:</u>

Cr is bcc, $a_o = 0.2884$ nm

$$\Rightarrow V_{Cr}^{\text{unit cell}} = a_o^3 = 0.024\text{ nm}^3\ (2\text{ atoms per unit cell});$$

$$\#\text{ of Cr unit cells, } N_{\text{unit cell}}^{Cr} = \frac{9.08\times10^{8}\text{ atoms}}{2\text{ atoms / unit cell}} = 4.54\times10^{8}\text{ Cr unit cells}$$

$$V_{tot}^{Cr} = V_{\text{unit cell}}^{Cr}\cdot N_{\text{unit cell}}^{Cr}$$

$$\Rightarrow V_{tot}^{Cr} = 0.024\text{ nm}^3\times4.54\times10^{8}\text{unit cells} = 1.09\times10^{7}\text{ nm}^3$$

Since a spherical precipitate is assumed the radius is taken as

$$r_{Cr} = \left[\frac{3V_{tot}^{Cr}}{4\pi}\right]^{\frac{1}{3}} = \left[\frac{3\cdot1.09\times10^{7}\text{ nm}^3}{4\pi}\right]^{\frac{1}{3}} \approx 137.5\text{ nm.}$$

For c = 100 K/s, $r_{Cr} \approx 137.5$ nm ($d_{Cr} \approx 275$ nm).

For c = 1000 K/s, $r_{Cr} \approx 43.3$ nm ($d_{Cr} \approx 86.6$ nm).

<u>Size of (possible) Nb Precipitates:</u>

Nb is bcc, $a_o = 0.33$ nm

$$\Rightarrow V_{Nb}^{\text{unit cell}} = a_o^3 = 0.035937\text{ nm}^3\ (2\text{ atoms per unit cell});$$

$$\text{\# of Nb unit cells, } N_{\text{unit cell}}^{\text{Nb}} = \frac{1.485\times10^{6}\ \text{atoms}}{2\ \text{atoms / unit cell}} = 7.425\times10^{6}\ \text{Nb unit cells}$$

$$V_{\text{tot}}^{\text{Nb}} = V_{\text{unit cell}}^{\text{Nb}} \cdot N_{\text{unit cell}}^{\text{Nb}}$$

$$\Rightarrow\ V_{\text{tot}}^{\text{Nb}} = 0.035937\ \text{nm}^3 \times 7.425\times10^{6}\,\text{unit cells} = 2.67\times10^{4}\ \text{nm}^3$$

Since a spherical precipitate is assumed the radius is taken as

$$r_{\text{Nb}} = \left[\frac{3V_{\text{tot}}^{\text{Nb}}}{4\pi}\right]^{\frac{1}{3}} = \left[\frac{3\cdot 2.67\times10^{4}\ \text{nm}^3}{4\pi}\right]^{\frac{1}{3}} \approx 18.5\ \text{nm}.$$

For c = 100 K/s, $r_{\text{Nb}} \approx 18.5$ nm ($d_{\text{Nb}} \approx 37$ nm).

For c = 1000 K/s, $r_{\text{Nb}} \approx 5.86$ nm ($d_{\text{Nb}} \approx 11.7$ nm).

Size of the predominant Cr_2Nb Precipitates:

Cr_2Nb is Laves phase C15 (cubic fcc), $a_o = 0.699$ nm

$$\Rightarrow\ V_{\text{Cr}_2\text{Nb}}^{\text{unit cell}} = a_o^3 = 0.34153\ \text{nm}^3$$ (24 atoms per unit cell);# of Cr_2Nb unit cells*,

$$N_{\text{unit cell}}^{\text{Cr}_2\text{Nb}} = \frac{2\times1.485\times10^{6} + 1.485\times10^{6}\text{atoms}}{24\ \text{atoms / unit cell}} = 1.856\times10^{5}\ \text{Cr}_2\text{Nb unit cells}$$

$$V_{\text{tot}}^{\text{Cr}_2\text{Nb}} = V_{\text{unit cell}}^{\text{Cr}_2\text{Nb}} \cdot N_{\text{unit cell}}^{\text{Cr}_2\text{Nb}}$$

$$\Rightarrow\ V_{\text{tot}}^{\text{Cr}_2\text{Nb}} = 0.34153\ \text{nm}^3 \times 1.856\times10^{5}\ \text{unit cells} = 6.34\times10^{4}\ \text{nm}^3$$

Again, since a spherical precipitate is assumed the radius is taken as

$$r_{\text{Cr}_2\text{Nb}} = \left[\frac{3V_{\text{tot}}^{\text{Cr}_2\text{Nb}}}{4\pi}\right]^{\frac{1}{3}} = \left[\frac{3\cdot 6.34\times10^{4}\ \text{nm}^3}{4\pi}\right]^{\frac{1}{3}} \approx \mathbf{24.7\ nm}.$$

For c = 100 K/s, $r_{Cr2Nb} \approx 24.7$ nm ($d_{Cr2Nb} \approx 50$ nm).

For c = 1000 K/s, $r_{Cr2Nb} \approx 7.8$ nm ($d_{Cr2Nb} \approx 15.6$ nm)

---

[*] Nb is considered rate limiting since its diffusivity is more than 20 times less than that of Cr. Thus, the sphere volume is based on $\overline{D}_{\text{Nb}}$, which is also why the number of Nb atoms are used.

Appendix 2B Average Diffusivities of Cr and Nb in Cu (based on Crank)

(For c = 100 K/s, but same for 1000 K/s)

Elapsed Time	Temp	Diffusivity of Cr in Cu	Diffusivity of Nb in Cu	DΔt' for Cr	DΔt' for Nb
(s)	(K)	(cm^2/s)	(cm^2/s)	(cm^2)	(cm^2)
4.72	784	3.486E-14	3.815E-17	1.867E-08	6.176E-10
4.73	783	3.356E-14	3.632E-17	1.832E-08	6.026E-10
4.74	782	3.230E-14	3.457E-17	1.797E-08	5.880E-10
4.75	781	3.108E-14	3.290E-17	1.763E-08	5.736E-10
4.76	780	2.991E-14	3.131E-17	1.729E-08	5.596E-10
4.77	779	2.878E-14	2.979E-17	1.696E-08	5.458E-10
4.78	778	2.769E-14	2.835E-17	1.664E-08	5.324E-10
4.79	777	2.663E-14	2.697E-17	1.632E-08	5.193E-10
4.8	776	2.562E-14	2.565E-17	1.601E-08	5.065E-10
4.81	775	2.464E-14	2.439E-17	1.570E-08	4.939E-10
4.82	774	2.370E-14	2.320E-17	1.539E-08	4.816E-10
4.83	773	2.279E-14	2.206E-17	1.510E-08	4.696E-10

$n = 483$ $\Delta t' = 0.01$ s

$$\Rightarrow \sum_{\Delta t=0}^{n} D_{Cr}(t')\Delta t' = 1.594 \times 10^{-9}\,\text{cm}^2$$

$$\Rightarrow \sum_{\Delta t=0}^{n} D_{Nb}(t')\Delta t' = 3.526 \times 10^{-11}\,\text{cm}^2$$

$$\Rightarrow \boxed{\overline{\mathbf{D}}_{Cr} = \frac{\sum_{\Delta t=0}^{n} \mathbf{D}_{Cr}(\mathbf{t}')\Delta \mathbf{t}'}{\sum_{\Delta t=0}^{n} \Delta \mathbf{t}'} = \mathbf{3.3 \times 10^{-10}\,cm^2 / s}}$$

$$\Rightarrow \boxed{\overline{\mathbf{D}}_{Nb} = \frac{\sum_{\Delta t=0}^{n} \mathbf{D}_{Nb}(\mathbf{t}')\Delta \mathbf{t}'}{\sum_{\Delta t=0}^{n} \Delta \mathbf{t}'} = \mathbf{7.3 \times 10^{-12}\,cm^2 / s}}$$

REPORT DOCUMENTATION PAGE

Form Approved
OMB No. 0704-0188

1. AGENCY USE ONLY (*Leave blank*)	**2. REPORT DATE** June 1996	**3. REPORT TYPE AND DATES COVERED** Final Contractor Report

4. TITLE AND SUBTITLE

High Temperature Coarsening of Cr_2Nb Precipitates in Cu-8 Cr-4 Nb Alloy

5. FUNDING NUMBERS

WU–466–03–02
C–77166–B

6. AUTHOR(S)

Kenneth Reed Anderson

7. PERFORMING ORGANIZATION NAME(S) AND ADDRESS(ES)

University of California at Davis
Davis, California 95616

8. PERFORMING ORGANIZATION REPORT NUMBER

E–10293

9. SPONSORING/MONITORING AGENCY NAME(S) AND ADDRESS(ES)

National Aeronautics and Space Administration
Lewis Research Center
Cleveland, Ohio 44135–3191

10. SPONSORING/MONITORING AGENCY REPORT NUMBER

NASA CR–198492

11. SUPPLEMENTARY NOTES

This report was submitted as a thesis in partial fulfillment of the requirements for the degree Master of Science to the University of California at Davis, California. Project Manager, Robert L. Dreshfield, Materials Division, NASA Lewis Research Center, organization code 5120, (216) 433–3267.

12a. DISTRIBUTION/AVAILABILITY STATEMENT

Unclassified - Unlimited
Subject Category 26

This publication is available from the NASA Center for AeroSpace Information, (301) 621–0390.

12b. DISTRIBUTION CODE

13. ABSTRACT ***(Maximum 200 words)***

A new high-temperature-strength, high-conductivity Cu-Cr-Nb alloy with a Cr:Nb ratio of 2:1 was developed to achieve improved performance and durability. The Cu-8 Cr-4 Nb alloy studied has demonstrated remarkable thermal and microstructural stability after long exposures at temperatures up to 0.98 T_m. This stability was mainly attributed to the slow coarsening kinetics of the Cr_2Nb precipitates present in the alloy. At all temperatures, the microstructure consists of a bimodal and sometimes trimodal distribution of strengthening Cr_2Nb precipitates, depending on precipitation condition, i.e. from liquid or solid solution, and cooling rates. These precipitates remain in the same size range, i.e. large precipitates of approximately 1 μm, and small precipitates less than 300 nm, and effectively pin the grain boundaries thus retaining a fine grain size of 2.7 μm after 100 h at 1323 K. (A relatively small number of Cr-rich and Nb-rich particles were also present.) This grain boundary pinning and sluggish coarsening of Cr_2Nb particles explain the retention of good mechanical properties after prolonged holding at very high temperatures, e.g., 75% of the original hardness after aging for 100 h at 1273 K. Application of LSW-based coarsening models indicated that the coarsening kinetics of the large precipitates are most likely governed by grain boundary diffusion and, to a lesser extent, volume diffusion mechanisms.

14. SUBJECT TERMS

Alloys; Copper; High temperature; Thermal conductors

15. NUMBER OF PAGES

63

16. PRICE CODE

A04

17. SECURITY CLASSIFICATION OF REPORT Unclassified	**18. SECURITY CLASSIFICATION OF THIS PAGE** Unclassified	**19. SECURITY CLASSIFICATION OF ABSTRACT** Unclassified	**20. LIMITATION OF ABSTRACT**

National Aeronautics and
Space Administration
Lewis Research Center
21000 Brookpark Rd.
Cleveland, OH 44135-3191